Nanoscale

Encapsulation of Metal Nanoparticles at the Surface of a Prototypical Layered Material

Journal:	*Nanoscale*
Manuscript ID	NR-REV-09-2020-007024.R1
Article Type:	Review Article
Date Submitted by the Author:	17-Dec-2020
Complete List of Authors:	Lii-Rosales, Ann; University of Colorado Boulder Han, Yong; Ames Laboratory Jing, Dapeng; Iowa State University, Materials Analysis and Research Laboratory Tringides, Michael; Iowa State University, Julien, Scott; Northeastern University Wan, Kai-Tak; Northeastern University, Department of Mechanical Engineering Wang, Cai Zhuang; Ames Laboratory-U.S. DOE, Physics and Astronomy Lai, King Chun; Iowa State University, Evans, James; Ames Laboratory Thiel, Patricia; Iowa State University and Ames Laboratory

Encapsulation of Metal Nanoparticles at the Surface of a Prototypical Layered Material

Ann Lii-Rosales,[a,b,@*] Yong Han,[a,c] Dapeng Jing,[a] Michael C. Tringides,[a,c] Scott Julien,[e] Kai-Tak Wan,[e] Cai-Zhuang Wang,[a,c] King C. Lai,[a,c,+] J.W. Evans,[a,c,*] and Patricia A. Thiel[a,b,d,#]

[a] Ames Laboratory of the USDOE, Ames, Iowa 50011 USA
[b] Department of Chemistry, Iowa State University, Ames, Iowa 50011 USA
[c] Department of Physics and Astronomy, Iowa State University, Ames, Iowa 50011 USA
[d] Department of Materials Science and Engineering, Iowa State University, Ames, Iowa 50011 USA
[e] Department of Mechanical Engineering, Northeastern University, Boston, MA USA
[@] Current address: Department of Chemistry, University of Colorado Boulder, Boulder, CO 80309 USA
[+] Current address: Fritz-Haber Institut der Max Planck Gesellschaft, Faradayweg 4-6, 14195 Berlin, Germany
[*] Authors to whom correspondence should be addressed: ann.lii.rosales@gmail.com, jevans@ameslab.gov
[#] Patricia A. Thiel passed away on September 7, 2020.

Key words: graphite, metal, intercalation, encapsulation, surface

Acronyms and nomenclature:

GML – Graphene monolayer
ML – Monolayer
EC – Encapsulated (metal) cluster
Nanoparticle or nanocluster – the metallic portion alone
Island or nanoprotrusion – the composite metallic portion plus its local graphitic surroundings, i.e., the top membrane consisting of one or more GMLs, and the graphitic substrate at the bottom
XPS – X-ray photoelectron spectroscopy
STM – Scanning tunneling microscopy
DFT – Density functional theory
BE – Binding energy (in XPS)
KMC – Kinetic Monte Carlo
Gn – Graphene
Gt – Graphite
CE – Continuum elasticity (model)
UHV – Ultrahigh vacuum
i-graphite – Graphite that has been ion bombarded and contains many surface defects
p-graphite – Pristine graphite, prepared without ion bombardment.
Graphene membrane – Graphene layer(s) that cover the encapsulated cluster.
Gallery – The space between two adjacent graphene sheets.

Variables:

T_{dep} – Sample temperature during deposition
N_{enc} – Areal density of encapsulated clusters

N_{def} – Areal density of defects induced by ion bombardment
r – Radial distance from the portal
$\langle r_{nuc} \rangle$ – Average radial distance at which nucleation occurs, relative to the portal
n – Number of atoms in a metal cluster
M – Type of metal
E_{tot} – Total energy of the metal-plus-graphite system
$E_{graphite}$ – Energy of graphite substrate
E_M – Energy of one metal atom in the gas phase
E_{ads} – Adsorption energy of a single metal adatom on top of the layered material
μ_M – Chemical potential of the metal
L_l – Number of monolayers of layered material
L_M – Number of monolayers of metal
m – Number of carbon atoms missing in a vacancy defect

Outline.

1. Introduction.
2. Characterization and structure.
3. Growth conditions and mechanism.
4. Potential role of carbon dissolution.
5. Defects as entry portals; comparison with steps.
6. Classes of systems.
7. DFT calculations of stability.
8. Predicting encapsulation.
9. Kinetics modeling.
10. Factors governing shapes of the nanoparticles.
11. Stability in air.
12. Conclusions.

Abstract

Encapsulation of metal nanoparticles just below the surface of a prototypical layered material, graphite, is a recently discovered phenomenon. These encapsulation architectures have potential for tuning the properties of two-dimensional or layered materials, and additional applications might exploit the properties of the encapsulated metal nanoclusters themselves. The encapsulation process produces novel surface nanostructures and can be achieved for a variety of metals. Given that these studies of near-surface intercalation are in their infancy, these systems provide a rich area for future studies. This Review presents the current progress on the encapsulation, including experimental strategies and characterization, as well as theoretical understanding which leads to the development of predictive capability. The Review closes with future opportunities where further understanding of the encapsulation is desired to exploit its applications.

1. Introduction.

There is strong interest in intercalation and encapsulation of elemental materials beneath surfaces of two-dimensional (2D) and layered materials. This derives from two main perspectives. The first is the optimization of the properties of the 2D and layered materials. Graphene and other 2D materials have many promising electronic and spintronic applications

based on their unusual band structures.[1, 2] Linear energy dispersions, the number of bands, the size of the band gap, effective electron masses, topological edge states, band splitting, band polarization and other band features can be tuned to grow quantum materials with well-defined properties for targeted applications. A very promising method to accomplish this tunability is metal intercalation, since one utilizes the electronic interaction between the intercalated metal and the 2D electron gas of graphene to selectively add specific terms in the graphene Hamiltonian thereby engineering the properties of interest.[3]

Graphene often exists in so-called 'few-layer' or multilayer form, largely as a result of the growth conditions of the material.[4] For instance, on SiC, it is common to grow more than one graphene sheet, atop a graphene-like buffer layer of carbon, because the number of layers is very sensitive to cooling rate. In other cases, multilayer graphene is produced deliberately by stacking graphene sheets. This has been done, for instance, to explore the superconducting properties as a function of the rotational angle between two graphene lattices.[5] Graphite is an excellent prototype for multilayer graphene.

The second perspective focuses on exploiting the properties of the intercalated or encapsulated metals themselves. The catalytic, magnetic, and photonic properties of metal nanoparticles are well known. Encapsulating them beneath a 2D material is one strategy to protect them from environmental degradation, such as oxidation, while retaining or even enhancing their useful properties.[6-9] Another advantage of encapsulation is that the morphology of the nanoparticle is forced into a relatively flat configuration, with high surface-to-volume ratio and good contact with the 2D material.[10, 11] This is advantageous for several applications, e.g., heat sinks and electrodes.

It has been discovered recently that transition metals Cu, Fe, Ru, and Pt, as well as the rare earths Dy and Gd, can be encapsulated as metallic nanoparticles at the surface of graphite.[12-17] The encapsulated clusters (ECs) are prepared and characterized in ultrahigh vacuum (UHV). Key conditions that enable the encapsulation are metal deposition on an ion-bombarded graphite (*i*-graphite) surface that is held at sufficiently high temperatures. Ion bombardment is required to create point defects that can act as portals for metal atoms to access the galleries (the space between adjacent graphene sheets) of the graphite substrate. High temperatures are required to facilitate detachment of atoms from metal clusters heterogeneously nucleated at surface defects, thereby allowing transport across the surface to portal defects, and ultimately access to the gallery. Technical details are provided in the original literature.[12-16] Note that typically about 10 monolayers (ML) of metal is deposited for Cu and Fe, and around or below 1 ML for Ru, Pt and Dy. The observation of surface encapsulation of these metals is somewhat surprising, given that there is no precedent for the transition metals to form bulk graphite intercalation compounds.[18, 19] In the one case where precedent does exist—for the rare earth Dy—features of Dy clusters embedded *at the graphite surface* depart significantly from those known for Dy embedded *in the graphite bulk*. One main difference is that Dy clusters at the surface consist of 3 metal layers,[12] whereas a Dy layer in the intercalation compound does not exceed a single layer in height. The transition metals can form even taller surface-encapsulated clusters, up to 200 metal layers for Cu.[13] Clearly, the forces and processes that lead to surface encapsulation are different than those that would lead to bulk intercalation.

The purpose of this paper is to review and summarize the recent work on metallic nanoclusters encapsulated at the surface of graphite, with an emphasis on the fundamental mechanism and driving force. Comparisons among the different metals lead to generalizations and classification into different categories. We begin by summarizing the evidence for their

existence, which is important, given that this is a new phenomenon. This is followed by an examination of various issues, including: requisite growth conditions; possible role of reactive carbon; defects as entry portals to the galleries; relative importance of kinetics and thermodynamics in EC formation; predictive capability; kinetic modeling; shapes (profiles); and stability in air. We close by discussing exciting open questions and possibilities for future work.

2. Characterization and structure.

Below, the following terminology will be used when referring to intercalated metal nanostructures. The term nanoparticle or nanocluster refers to the metallic portion alone. The term island refers to the composite structure forming a nanoprotrusion consisting of metallic portion plus its local graphitic surroundings. The latter consists of the top membrane consisting of one or more GMLs (graphene monolayers), and the graphitic substrate at the bottom (in the vicinity of the metallic portion.) There are essentially four lines of evidence for surface-encapsulated, multilayer metal nanoclusters: (i) their stability during STM imaging; (ii) observation of the carbon lattice and related moiré structures on top of the islands; (iii) the faceted footprints of the islands and their heights; and (iv) XPS data showing that the intercalated nanoclusters are metallic in nature.

Stability during STM imaging. Bonding of a metal with graphite or graphene surfaces is generally weak, compared with the strength of metal-metal bonding (cohesive energy). This has been expressed as a useful rule of thumb, in fact, to rationalize the fact that most metals grow three-dimensionally on graphite and graphene surfaces, as opposed to more two-dimensional growth (wetting).[20-23] Adsorption bond strengths, E_{ads}, for single metal atoms on graphite, calculated with DFT,[24] are summarized in Table I, together with cohesive energies for comparison.[25] It is interesting to note that, in Table I, the metal with the highest ratio of E_{ads} to cohesive energy is Dy, and this is also the only metal that exhibits a growth mode somewhat resembling 2D, i.e., flat and stable islands, albeit consisting of 3 Dy MLs (monolayers).[26]

Table I. Tabulation of the adsorption energy of a single metal atom (E_{ads}) on top of a graphite surface, from DFT. The adsorption site nomenclature is defined as follows: t indicates that the metal atom is on top of the surface; the first capital letter defines the site with respect to the first carbon layer, and the second capital letter does so with respect to the second carbon layer. Sites are shown in Fig. 1.

Metal	E_{ads}, eV	Preferred adsorption site	Source of E_{ads}	Cohesive energy, eV[25]
Ag	-0.283	tTH	[16]	2.95
Au	-0.492	tTH	[16]	3.81
Cu	-0.500	tTH	[13]	3.49
Fe	-0.934	tHT	[15]	4.28
Dy	-1.794	tHT	[24]	3.04
Pt	-1.813	tBM	[16]	5.84
Ru	-1.889	tHT	[14]	6.74

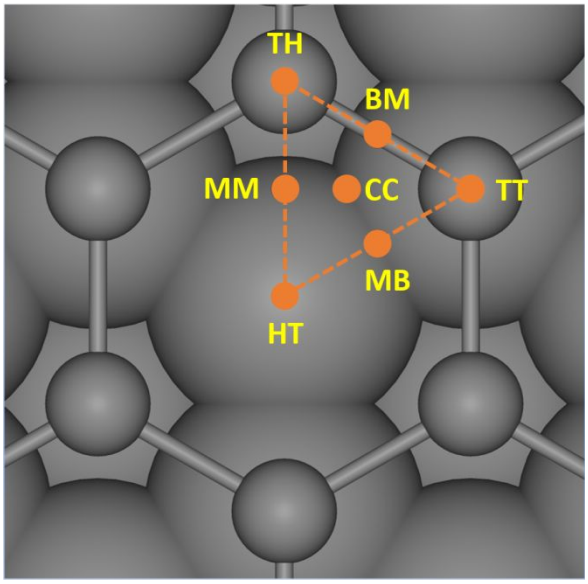

Figure 1. Top view of seven different positions (orange dots) considered in DFT calculations of single-metal-atom adsorption on graphite. Small gray circles represent the top graphene layer, and large circles represent the second graphene layer. The letters T, H, M, B, and C stand for top, hollow, midpoint, bridge, and center, respectively. The first letter signifies the adatom's position with respect to the top graphene layer, and the second letter does so with respect to the second graphene layer. Figure reprinted from Phys. Rev. Research **2**, 033175.

The weakness of the bond between the metal and graphite/graphene, plus the 3D nature of the cluster, often means that adsorbed metal clusters on top of the graphite surface are easily displaced by the tip during STM imaging. This is manifest as streaking in the direction of the scan, as shown in Fig. 2. The streakiness is observed even for metals on *i*-graphite where most metal clusters are anchored at defect sites due to heterogeneous nucleation.[27] This streakiness is more pronounced and prevalent for the metals with smaller values of E_{ads} in Table I. When it occurs, it is a valuable tool for distinguishing between adsorbed clusters and ECs, because in contrast the ECs are extremely stable during STM imaging. For example, Fig. 2(a) shows both types of clusters in the same image, and the difference is striking.

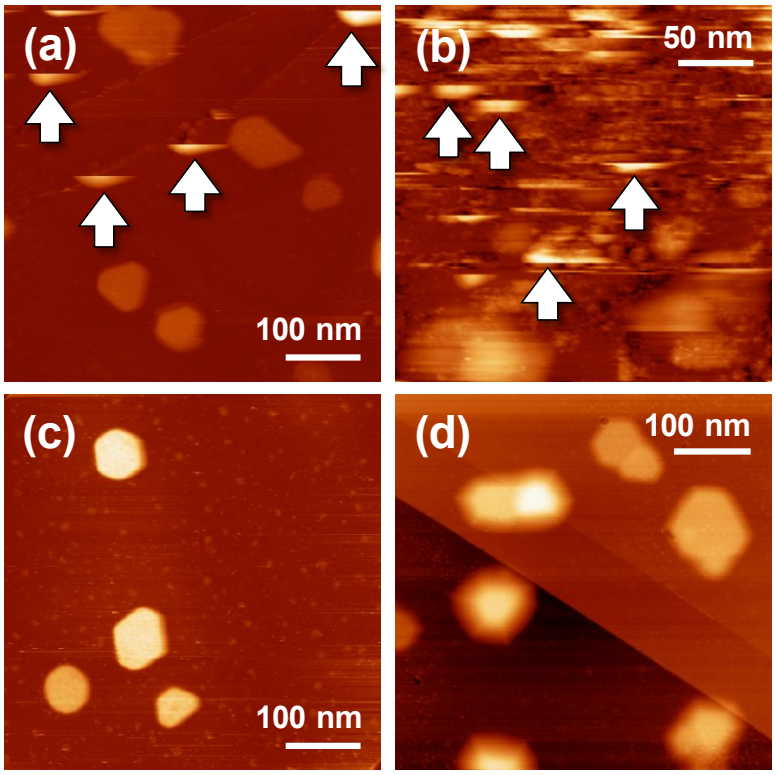

Figure 2. Topographic STM images of adsorbed (a) Fe clusters and (b) Cu clusters as indicated by arrows. For comparison, (c) and (d) show encapsulated Fe and Cu islands, respectively. Image source: (a, c) Reprinted from A. Lii-Rosales *et al*., Journal of Vacuum Science & Technology A, 37, 061403, (2019), with the permission of AIP Publishing. (b, d) Reprinted with permission from J. Phys. Chem. C, 2018, 122, 8, 4454-4469. Copyright 2018 American Chemical Society.

Observation of the carbon lattice and related moiré structures on top of encapsulated islands. Perhaps the strongest evidence for encapsulation is the consistent observation of the carbon lattice on top of the clusters that are most stable in STM imaging. Examples are shown in Fig. 3. A triangular lattice of protrusions is most commonly observed, with measured spacing 0.247 ± 0.003 nm,[12-16] which agrees well with the in-plane lattice constant of bulk graphite, 0.246 nm.[19, 28] Structurally, in a single GML, the carbon atoms are arranged in a honeycomb lattice, not a triangular one. However, on the surface of bulk graphite, the triangular lattice is attributed to A-B-A stacking of GMLs, which produces two inequivalent, triangular sublattices of C atoms in a given sheet.[29-31] On metal surfaces, interaction of a (hexagonal) metal surface with a graphene overlayer can also break the carbon lattice symmetry and cause graphene to be imaged as a triangular lattice in specific locations, as discussed below.[32, 33]

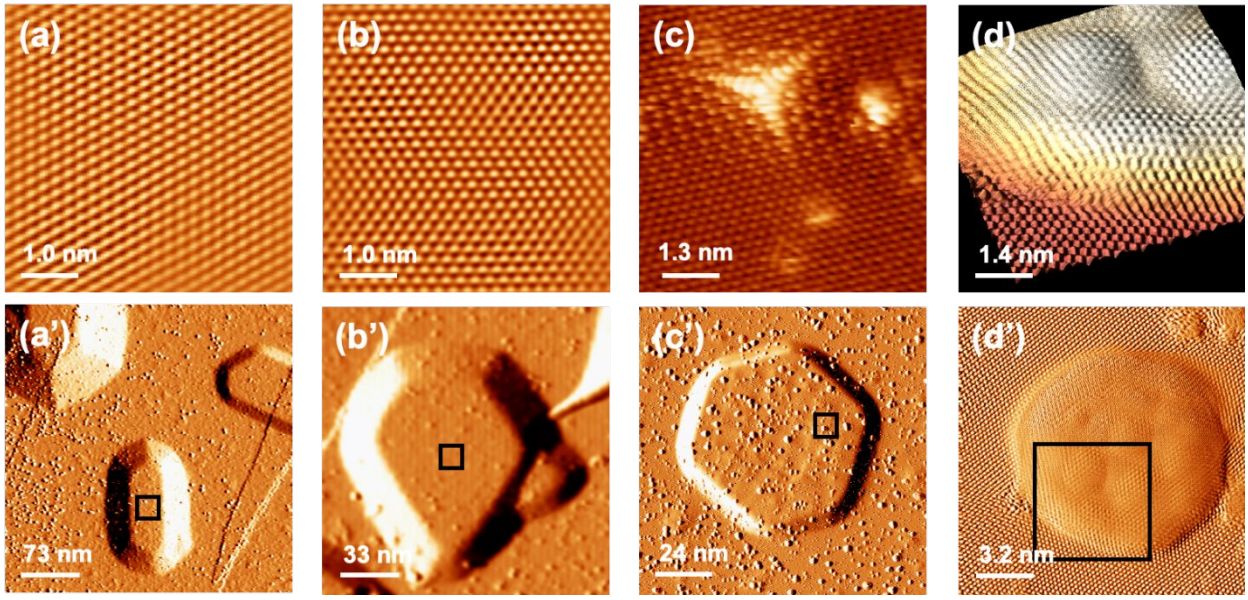

Figure 3. (a-d) Carbon lattice resolved in the select area on top of encapsulated (a', b') Cu islands (c') Fe island, and (d') Ru island. Small, particle-like features on top of the encapsulated islands and on the substrate are clean defects from ion bombardment, or defects that are decorated with bare metal atoms. Images source: (a, a', b, b') Reprinted with permission from J. Phys. Chem. C, 2018, 122, 8, 4454-4469. Copyright 2018 American Chemical Society. (c, c') Reprinted from A. Lii-Rosales *et al*., Journal of Vacuum Science & Technology A, 37, 061403, (2019), with the permission of AIP Publishing. (d, d') Nanotechnology 29 (2018) 505601.

Notably, the carbon lattice can be observed continuously across the EC, on the sides, and onto the surrounding graphite as shown in Fig. 3(d). In other words, the top graphene membrane drapes over the EC like a blanket. An interesting issue, which will be addressed below and elsewhere, is the number of GMLs which make up this membrane. Currently known values are summarized in Table II.

Table II. Summary of key characteristics of encapsulated multilayer metal islands on graphite. For Cu, both round- and flat-topped ECs[13] are included. N_{enc} is the areal density of ECs, and N_{def} is the areal density of defects from ion bombardment. Reprinted from A. Lii-Rosales *et al*., Journal of Vacuum Science & Technology A, 37, 061403, (2019), with the permission of AIP Publishing.

Metal	Average (range) of heights, in metal atomic layers	Average (range) of widths of flat tops, nm	Number of graphene layers in top membrane	Maximum N_{enc}, μm^{-2}	Ratio of N_{enc}/N_{def}	Ref.
Fe	13 (6-60)	50 (17-140)	> 1	12	$(1\text{-}6) \times 10^{-4}$	15
Cu	35 (10-200)	76 (30-570)	> 1	55	$(4\text{-}8) \times 10^{-3}$	13
Ru	3 (2-4)	13 (8-18)	1	600	5×10^{-2}	14
Dy	3	16 (7-34)	?	230	1×10^{-2}	12
Pt	4 (3-5)	no flat tops	?	36	2×10^{-3}	16

For graphene adsorbed on hexagonal surfaces of bulk metals, coincidence lattices, also called moiré patterns or moiré superlattices, are frequently observed. Their underlying cause is

the lattice mismatch between a GML and the metal: Equivalent positions in the superlattice occur periodically when different integral numbers of fundamental unit cells in the carbon and metal layers span the same real-space distance in a common direction. The moiré superlattice can be imaged in STM because it is corrugated, as shown in Fig. 3(d, d'). Such superlattices have been reported for graphene on bulk Cu(111),[34-36] Ru(0001),[32, 33, 37-40] Pt(111),[41-43] and other metals.[20, 43-46]

Among the encapsulated metals, the moiré superlattice has been observed atop Ru and Dy islands. On Ru, it is very similar to that of graphene atop bulk Ru(0001), thus providing strong evidence that the encapsulated Ru clusters are very similar to bulk Ru, with the top metal plane being hexagonally-close-packed. In fact, a quantitative analysis of the superlattice constant and its angle of rotation on encapsulated Ru yields a lattice constant for the underlying metal of 0.269 ± 0.003 nm, very close to the bulk Ru value of 0.271 nm.

Closer inspection of the moiré on encapsulated Ru clusters reveals another similarity. As shown in Fig. 4, the carbon lattice appears triangular in the lower regions, and honeycomb in the higher regions of the corrugation. (The nature of the corrugation—electronic or structural—has been debated,[47, 48] but the debate appears to have been settled in favor of structural corrugation, at least for Ru.[40]) This variation in carbon lattice appearance has been observed also for GML/Ru(0001). The triangular lattice is attributed to strong graphene interaction with the hexagonal Ru surface, which breaks the six-fold symmetry, whereas the honeycomb lattice is attributed to weak interaction with the underlying metal. The fact that this distinctive characteristic is observed for encapsulated Ru reinforces the conclusion (above) that the Ru presents a surface that is very similar to Ru(0001), and also indicates that the graphene is a single monolayer. Thicker graphene layers extinguish this feature.[32, 33]

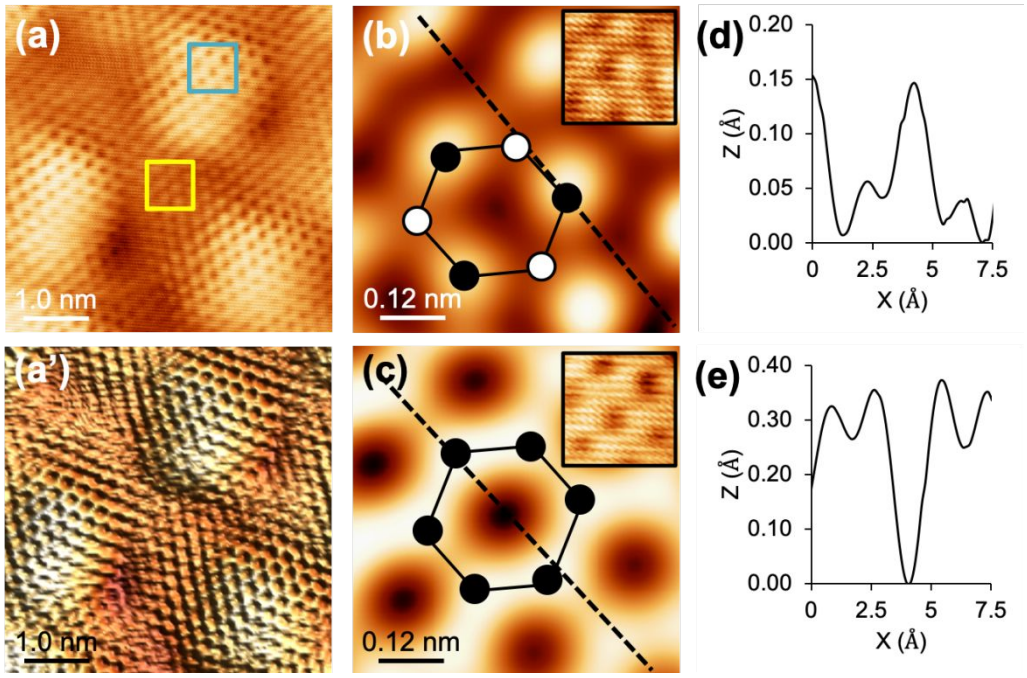

Figure 4. High-resolution images of moiré patterns on top of an embedded Ru island formed at 1050 K. (a) Moiré corrugations with different appearance of the C lattice depending on its location relative to the moiré. The lower (yellow) box sits at a moiré minimum, which shows triangular arrays of C lattice (3 out of 6 C atoms) with its enlargement further shown in (b). The top (blue) box sits at a moiré maximum where the C lattice is imaged as honeycombs (all 6 C atoms are equally imaged); (c) shows its enlargement. A semi-three-dimensional view is shown

in (a′), where the hollow honeycombs are very visible around moiré maxima. (d), (e) Shows distinct profiles along diagonal dashed lines in (b), (c) for different appearance of the C lattice. (a) is topographic. (b) and (c) are Fourier-filtered, while their insets show corresponding topographic images. Image source: Nanotechnology 29 (2018) 505601.

However, moiré patterns are not observed for encapsulated Cu, Fe and Pt islands, even though they have been reported for GMLs grown on the corresponding bulk metal surfaces in the case of Cu and Pt. There are several possible reasons. For Pt, the encapsulated islands are not flat-topped, which precludes a moiré. In the case of Cu, many islands have flat tops but there is evidence that the top graphene layer is several layers thick, which would dampen or extinguish the corrugation. Defects (Sec. 3) may also interfere with the development of the moiré.

Faceted footprints of islands and their heights. A general feature of the ECs is their faceted footprints. Examples are shown in Fig. 5. The footprints are usually hexagonal or distorted hexagonal, indicating that the islands are single crystals with a hexagonal close-packed plane parallel to the graphite surface. One exception is Fe, which exhibits a variety of footprints that evolve with T_{dep}, suggesting a progression from fcc-Fe to bcc-Fe.[15] The hexagonal shape shown in Fig. 5(a) is associated with fcc-Fe. Other exceptions are Cu[13] and Pt,[16] for which *some* or *all* ECs have round tops with round (unfaceted) footprints, respectively. Examples of these round islands are also shown in Fig. 5(e, f).

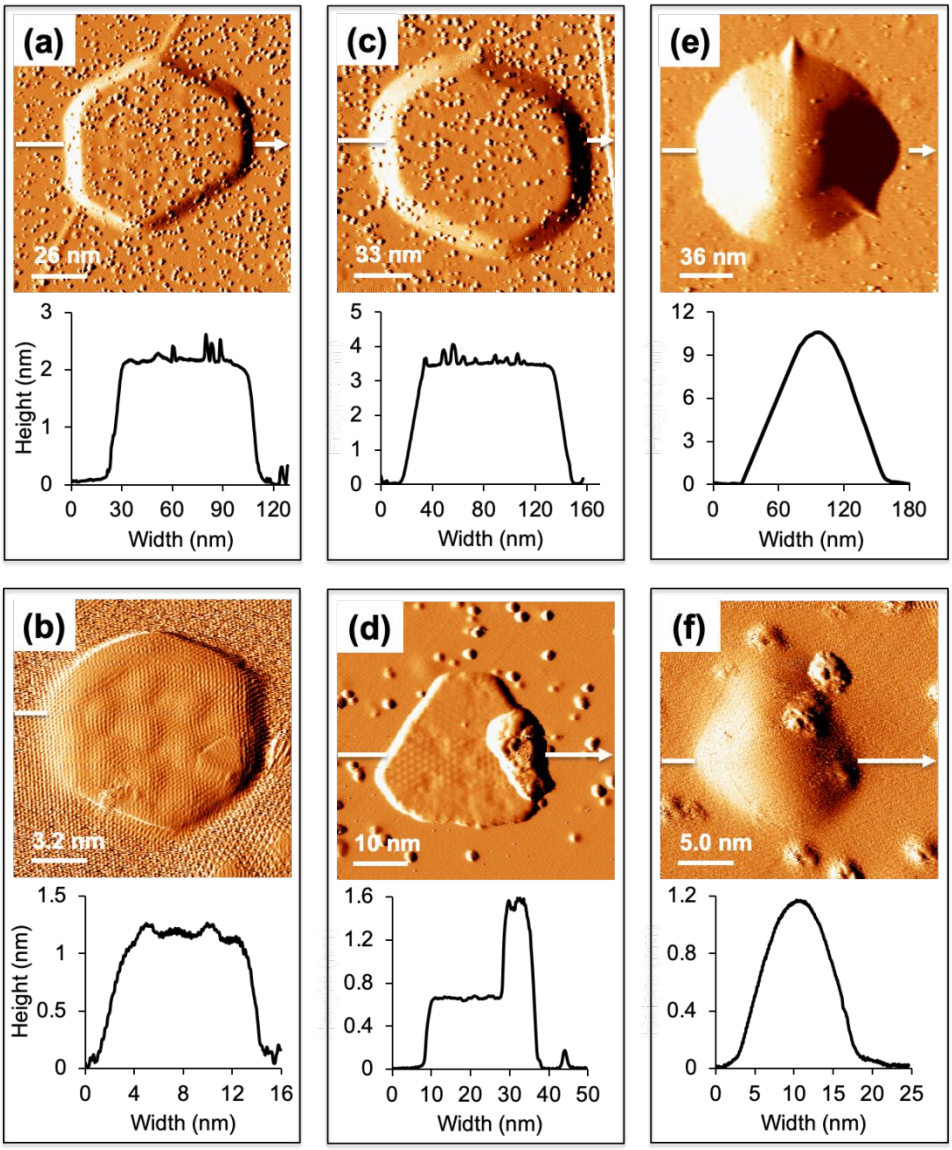

Figure 5. Comparison of footprints of ECs and their associated profiles. ECs that exhibit faceted footprints: (a) Fe, (b) Ru, (c) Cu, and (d) Dy. Exceptions of rounded footprints exhibited by (e) Cu and (f) Pt ECs. Small, particle-like features on top of the encapsulated islands and on the substrate are clean defects from ion bombardment, or defects that are decorated with bare metal atoms. Image source: (a) Reprinted from A. Lii-Rosales *et al.*, Journal of Vacuum Science & Technology A, 37, 061403, (2019), with the permission of AIP Publishing. (b) Nanotechnology 29 (2018) 505601. (c) Reprinted with permission from J. Phys. Chem. C, 2018, 122, 8, 4454-4469. Copyright 2018 American Chemical Society. (d) Reprinted from Carbon, 127, 305-311, Zhou *et al.*, Defect-mediated, thermally-activated encapsulation of metals at the surface of graphite, Copyright (2018), with permission from Elsevier. (f) Phys. Rev. Research 2, 033175, 2020.

The heights of ECs indicate that they consist of metal *multilayers*. The shortest islands are Dy and Ru, with heights of 0.6 nm (3 Dy monolayers) and 0.4-1.0 nm (2-4 Ru monolayers), respectively. Cu is the tallest, with heights reaching up to 35 nm (ca. 200 Cu monolayers). Heights are summarized in Table II. Finally, it is noteworthy that in any given system, the range of heights for the ECs is distinct from the range of heights for adsorbed clusters.

XPS data. Finally, XPS data confirm that the ECs are *metallic* in nature. This is based on the invariant XPS peak positions (binding energies, or BEs) and widths as a function of T_{dep},

starting from low temperature (300 K) where adsorbed clusters exist that are undoubtedly metallic in nature, to higher temperature where ECs predominate. Examples are shown in Fig. 6. The BEs are also consistent with literature values for the bulk metals.

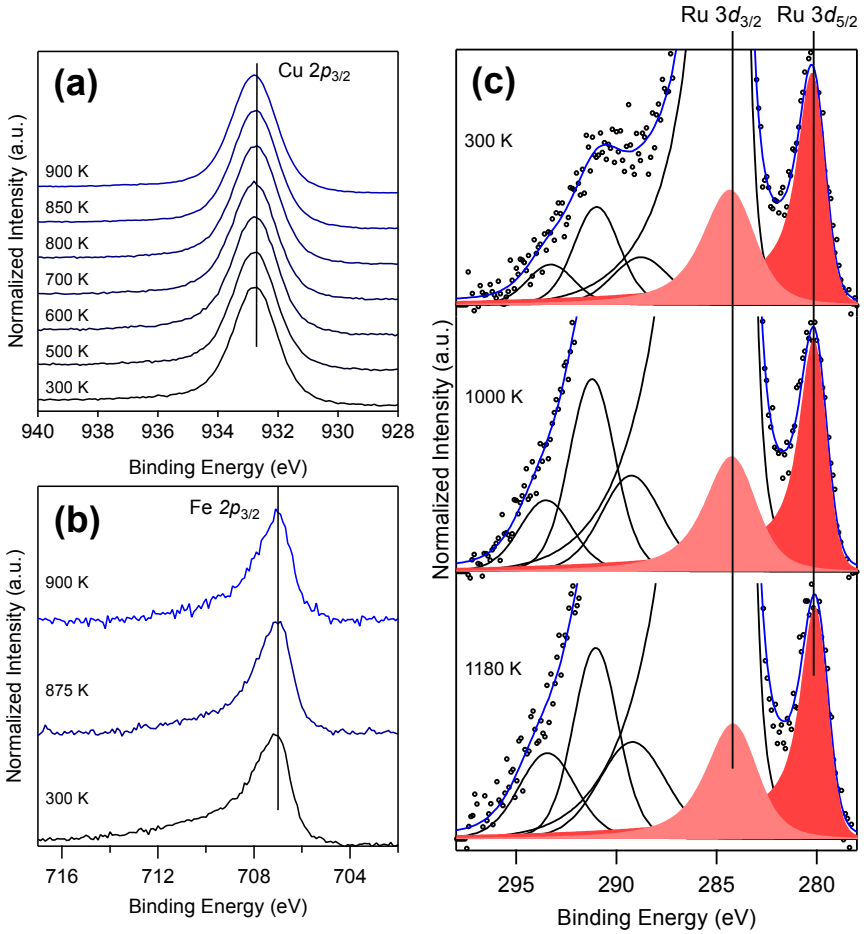

Figure 6. XPS spectra of (a) Cu, (b) Fe and (c) Ru deposited on *i*-graphite at various deposition temperatures. The vertical lines show the average binding energy of Cu $2p_{3/2}$, Fe $2p_{3/2}$, Ru $3d_{3/2}$ and Ru $3d_{5/2}$ peaks at 932.7, 707.0, 284.1 and 280.0 eV. Solid black curves in (c) show the C 1*s* main peak (truncated) and its loss features. Solid blue line in (c) shows the overall fit to the experimental data points. Intensities are normalized. Image source: (a) Reprinted with permission from J. Phys. Chem. C, 2018, 122, 8, 4454-4469. Copyright 2018 American Chemical Society. (c) Nanotechnology 29 (2018) 505601.

We summarize the conclusions of this section as follows.

- Evidence that ECs are encapsulated lies in the observation of a continuous carbon lattice at the surface.
- ECs are distinguished from adsorbed clusters based upon their stability under tunneling conditions in STM, as well as their heights.
- Evidence that the ECs are crystalline, with a close-packed plane parallel to the graphite surface, comes from their typical quasi-hexagonal shapes and flat tops (though some exhibit round tops). In the case of Ru, additional evidence comes from the close resemblance between the moiré structure observed on the ECs, and that reported for GML/Ru(0001), plus quantitative analysis of the lattice constant of the underlying metal.

- ECs are metallic, based upon XPS data (as well as the evidence, cited above, that they are crystalline.)
- ECs consist of metal multilayers based on their heights.

To help summarize these characteristics, a simple schematic of the structure of a flat-topped EC is shown in Fig. 7.

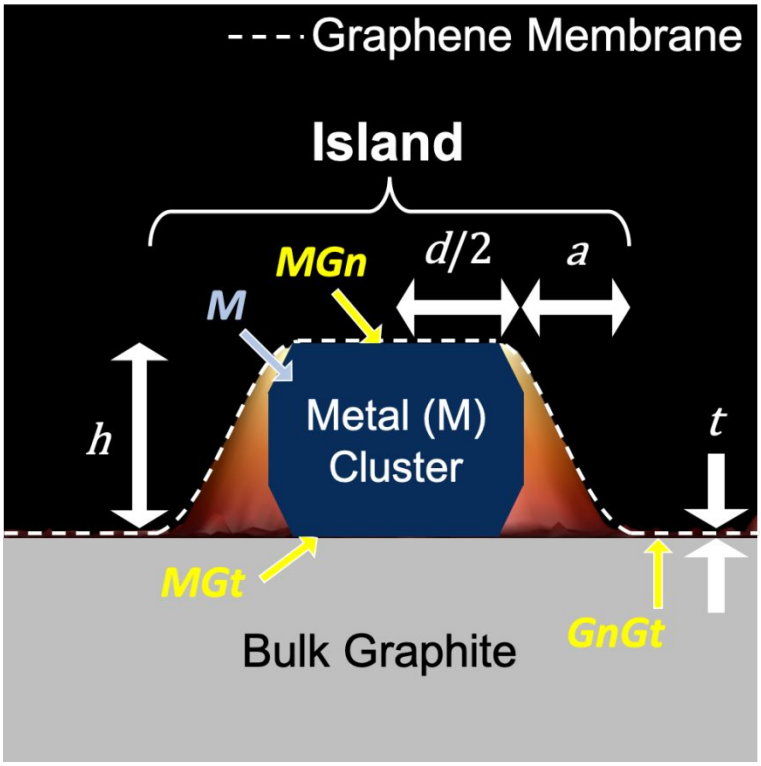

Figure 7. Schematic of the structure of a flat-topped EC. Labeled dimensions are height (h), diameter (d), width of annulus (a), and thickness of the graphene membrane (t). Surfaces and interfaces are also labeled as metal (M), metal-graphene (MGn), metal-graphite (MGt), and graphene-graphite (GnGt). Image adapted from Ann Lii-Rosales *et al*. 2020 New J. Phys. 22 023016.

3. Growth conditions and mechanism.

Growth conditions. Two specific conditions must be met to produce the ECs described in Sec. 2. First, defects in the surface of graphite must be created to act as entry portals to the galleries. This can be achieved by bombarding the surface with energetic Ar^+ ions, prior to metal deposition. Second, the sample must be held at elevated temperature during deposition.

Fig. 8 illustrates these two requirements for Pt. When Pt is deposited on *i*-graphite at T_{dep} ≤ 800 K, no ECs are observed (Fig. 8(a-b)), but they do appear at or above 950 K. Thus, a minimum value of T_{dep} is necessary to produce ECs, even when defect sites are plentiful. Furthermore, when the surface is held at elevated T_{dep} but is pristine (Fig. 8(g)), no ECs appear. There are only a few adsorbed clusters at the step edges. This shows that defect sites are essential, *as well as* elevated T_{dep}. Results are very similar for the other metals that form ECs – Cu, Fe, Ru, and Dy.

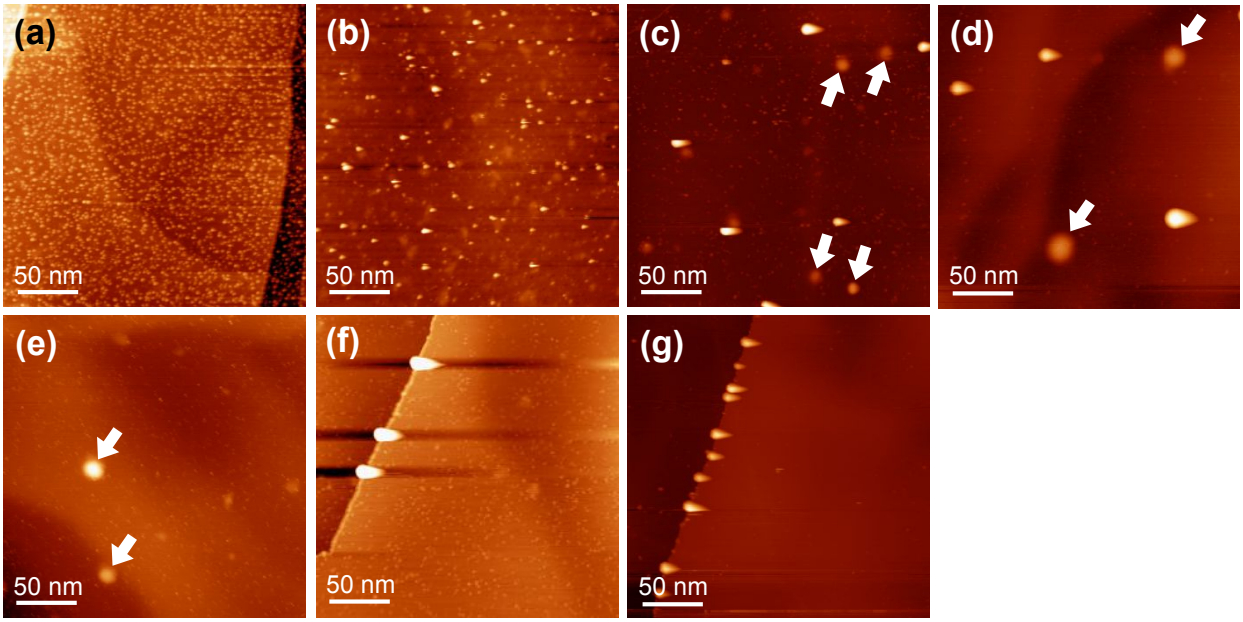

Figure 8. STM images after seven separate depositions of Pt on *i*-graphite at (a) 300 K, (b) 800 K, (c) 950 K, (d) 1000 K, (e) 1050 K, and (f) 1100 K, and on *p*-graphite (pristine graphite) at (g) 1000 K. Examples of Pt ECs are marked by arrows. Figure reprinted from Phys. Rev. Research 2, 033175, 2020.

There is usually a value of T_{dep} at which adsorbed clusters coexist with ECs, as in Fig. 8(c). Somewhat above that point, the areal density of adsorbed clusters falls but the areal density of ECs remains high or even increases. As temperature increases even further, all the features on terraces disappear (Fig. 8(f)). One can define the optimal deposition temperature as that which roughly maximizes the EC density and minimizes the adsorbed cluster density on terraces. Fig. 9 shows that there is a good linear correlation between the optimal values of T_{dep} and the cohesive energy[25] of the metal.[16]

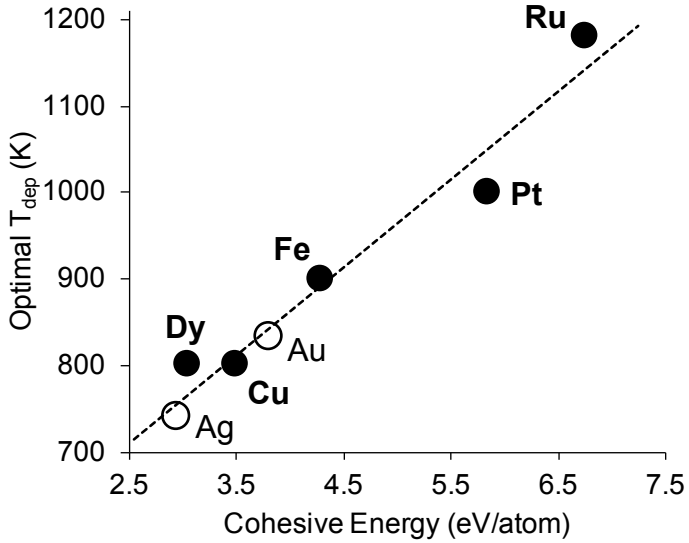

Figure 9. Optimal T_{dep} vs. cohesive energy. Data points (black circles) show transition metals Cu, Fe, Ru, and Pt and the rare earth Dy. Open circles show predictions for transition metals Ag and Au. Dashed line shows linear best fit

to the four data points, described by y = 102x + 435 and $R^2 = 0.96$. Figure adapted from Phys. Rev. Research 2, 033175, 2020.

Mechanism. Overall, the proposed mechanistic picture is as follows. Metal atoms adsorb on the surface, diffuse, then either undergo heterogeneous nucleation and growth of metal clusters at defect sites, or pass through the defects into the underlying graphite galleries. In the galleries they diffuse, nucleate and grow into ECs. This mechanism is discussed more fully in Sec. 9. In this picture, the elevated T_{dep} is necessary to facilitate detachment of metal atoms from clusters at defects enabling them to reach the portal (where facile detachment also prevents the portals from becoming clogged by adsorbed metal clusters during deposition). This is consistent with the correlation between cohesive energy and optimal T_{dep}.

A key element is the population of free metal adatoms in the gallery, relative to the population on top of the surface. If there is a quasi-equilibrium between the two phases (if passage through the portals is facile), this relative population is controlled by $\Delta\mu_M$, the difference in chemical potential between the two metal adatom phases. More specifically,

$$\Delta\mu_M = \mu_{M,\,intercalated} - \mu_{M,\,adsorbed} \quad (1)$$

(The chemical potential itself, as it is used in DFT, is defined in Sec. 7.) Note that a negative value of $\Delta\mu_M$ favors the presence of metal atoms in the gallery. A high density of metal adatoms in the gallery promotes nucleation there. This, and other mechanistic details, such as the dynamics of passage through the portals and the possible role of EC diffusion, are discussed elsewhere in this review. An alternative mechanism, involving carbon dissolution, is considered in Sec. 4.

Adsorption dynamics. Adsorption is part of the mechanistic picture described above, but there is evidence that adsorption dynamics are non-trivial under the relevant growth conditions. XPS consistently shows that the amount of metal on the surface falls as T_{dep} increases, starting from 300 K, even with constant total deposition flux. This is qualitatively confirmed by inspection of STM images, such as those in Fig. 8(a-f). In other words, the condensation coefficient σ decreases. (The condensation coefficient[49] is defined as the amount that is stably adsorbed on the surface, relative to the time-integrated flux.) A number of authors have reported that, even at 300 K, $\sigma < 1$ for a variety of metals on pristine graphite (*p*-graphite),[50] including Cu,[51] Ag,[52] Au[53] and Pt.[54] The decrease in σ with increasing T_{dep} may be caused by the onset of active desorption (at the higher end of the T_{dep} range), or a temperature-dependent sticking coefficient (at the lower end of the T_{dep} range).[50]

Summary. To summarize this section, both ion-bombardment-induced defects, and elevated T_{dep}, are necessary to produce ECs. These and other observations are consistent with a mechanism that involves adsorption, passage through portals, and diffusion and nucleation of metallic nanoclusters both atop and within galleries.

4. Potential role of carbon dissolution.

Dissolution-precipitation mechanism. Several of the metals that form ECs—notably Fe, Dy, and Ru—have high affinities for carbon. Since excess free carbon is likely present on the *i*-graphite surfaces as a result of ion bombardment, it is reasonable to consider the possibility that the mechanism of EC formation involves reaction of the metal with carbon. This is particularly true, since a well-known mechanism for graphene growth on bulk Fe and Ru (and other metals) exploits the high solubility of carbon at elevated temperatures, and the propensity for surface

precipitation upon cooling. For example, for Ru, the protocol is to heat the metal to elevated temperatures (1000-1400 K). During cooling, carbon segregates to the surface and forms graphene if the carbon concentration is sufficiently high.[32, 55-57] One thus might envision a mechanism for EC formation, whereby carbon is dissolved in the EC during growth at elevated temperature, and a graphene overlayer then forms when the sample is cooled to room temperature for observation.

This mechanism is, however, unlikely for several reasons. Considering again Ru as an example, adsorbed Ru clusters should be a precursor to the ECs, but the data do not show any obvious correlation between the two features.[14] Another observation is that the graphene membrane is continuous from the graphite surface, up and over each EC (as shown in Fig. 7). There is no reason why a graphene membrane, grown independently of the graphite substrate, should blanket the EC contiguously as observed. Finally, the amount of C dissolved, if any, in the supported cluster (versus a bulk metal substrate) should be insufficient to form a blanketing graphene sheet. These observations make the dissolution-precipitation mechanism unlikely.

Carbides. Carbide formation must also be considered, particularly for Fe and Dy. However, for both metals, there is evidence that carbide does not form under the conditions where ECs predominate. For Dy, the evidence comes from an STM study in which Dy-C formation was signaled by etch pits forming around the Dy islands, as a result of C consumption, and rough striations on island tops.[58] No such etch pits or striations are observed for the Dy ECs. For Fe, the evidence comes from XPS data in which a peak characteristic of Fe-C is absent.[15]

5. Defects as entry portals; comparison with steps.

Discovery of defects as portals. The idea of creating artificial surface defects to promote encapsulation or intercalation was pioneered by Büttner *et al*.,[59] who discovered that surface intercalation of Cs on graphite could be promoted in this way. The Cs islands are shown in Fig. 10. However, there were also differences between Cs and the metals emphasized in this review. One is that the surface-intercalated Cs characterized by Büttner *et al*. resembled the bulk graphite intercalation compound of Cs, having a thickness of a single Cs layer within a given gallery, rather than being a multilayer metallic island.

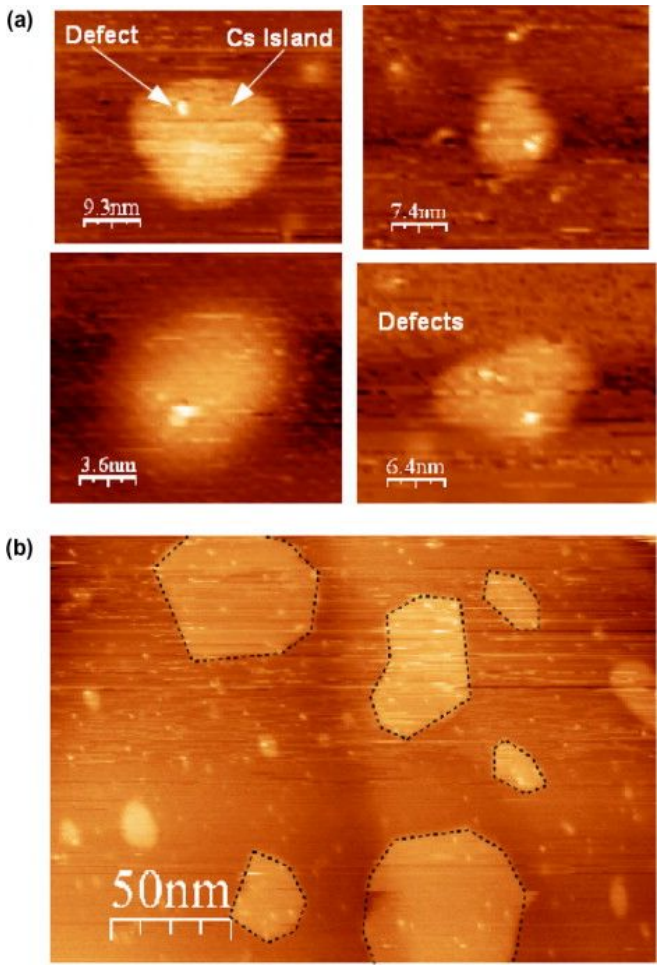

Figure 10. Cs intercalation in graphite. Image reprinted from Carbon, 49, 3937-3952, Büttner, *et al*., Vacancy clusters as entry ports for cesium intercalation in graphite, Copyright (2011), with permission from Elsevier.

Types and efficacies of defect portals. Fig. 11 shows STM images of both p- and i-graphite. The bright features in Fig. 11(c-g) are defects introduced by ion bombardment. From visual inspection of the shapes and intensities of these features, it is clear that many different types of defects exist. Previous studies have documented structural vacancies, interstitial carbon, and lattice distortions.[60-63] In addition, we see features that are known to signal specific structural vacancies, i.e., the 3-fold star in Fig. 11(e) is associated with a 1-atom vacancy, and the 4-fold feature in Fig. 11(f) with a 2-atom vacancy.[64-67] Moreover, the well-known[68-71] $(\sqrt{3}\times\sqrt{3})R30^{o}$ superstructure can be observed surrounding many defect sites and extending several nanometers, as shown in Fig. 11(g).

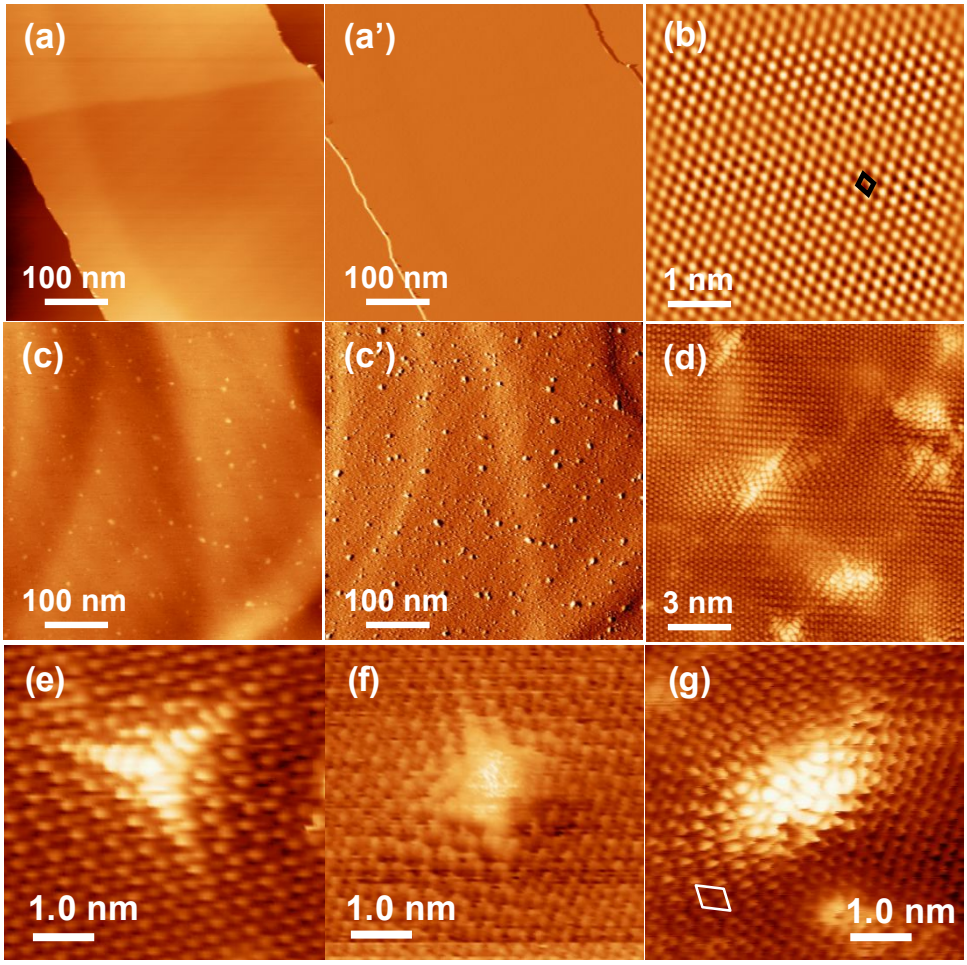

Figure 11. STM images of *p*- and *i*-graphite. (a) Topographic and (a') derivative images of p-graphite, low magnification. (b) Topographic image at high magnification, revealing the carbon lattice. (c) Topographic and (c') derivative images of *i*-graphite at low magnification. (d) Topographic image at high magnification. (e, f) Topographic images of 1-atom vacancies. (g) Topographic image of 2-atom vacancy. (h) Topographic image of a defect surrounded by the $(\sqrt{3} \times \sqrt{3})R30°$ superlattice. Images source: (a-d, f) Reprinted with permission from J. Phys. Chem. C, 2018, 122, 8, 4454-4469. Copyright 2018 American Chemical Society. (e) Reprinted from A. Lii-Rosales *et al*., Journal of Vacuum Science & Technology A, 37, 061403, (2019), with the permission of AIP Publishing.

Experiments consistently show that the areal density of ECs (N_{enc}) is several orders of magnitude lower than the density of all defects in the graphite surface (N_{def}) (Table II). Undoubtedly, some types of defects are less active than others for creating ECs; intuitively, one expects structural vacancies to be most effective for allowing atoms to pass from the surface into the galleries. Even among structural vacancies, however, efficiencies can differ based on size, for instance. In their DFT work, Büttner *et al*. showed that more than 4 neighboring C atoms in a graphene sheet must be missing, in order to obtain a reasonable activation barrier for Cs passage through the defect.[59] More recently, Yu *et al*. reported that the barrier for a Dy atom to pass through a graphene vacancy decreases with increasing number of missing C atoms, *m*, falling sharply from 2 eV at $m = 2$, to 0.3 eV at $m = 3$.[72]

The effectiveness of a portal likely depends not only on size, but on the arrangement of C atoms around its perimeter. The most stable C atom configurations at graphene vacancies can usually be described as mixtures of 5- and 6-membered C rings surrounding a larger hole. Some

vacancies also contain coordinatively-unsaturated C atoms (cus-C atoms).[62, 73-76] Examples are shown in Fig. 12.

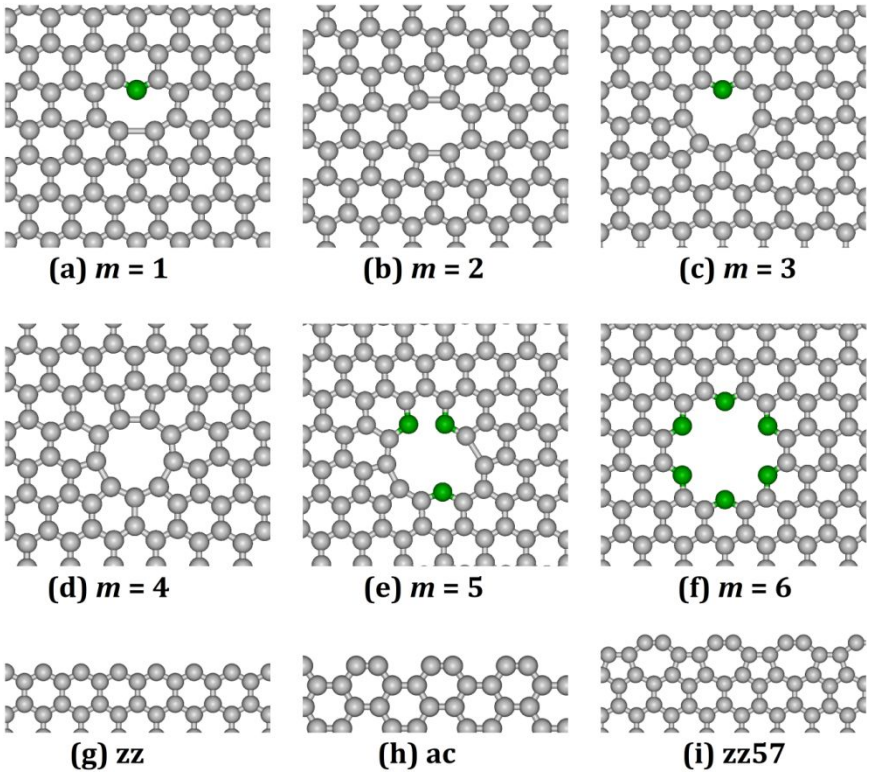

Figure 12. Structures (top views) of graphene vacancies and steps.[77] Gray balls are C atoms in the graphene layer, bonded to three others; green balls are cus-C atoms. In (a-f), m is the number of missing C atoms. For a given m, more than one configuration is possible.[62, 74, 78] Here we only show the arrangement with the largest central hole for each m. In (g-h), the two most common types of unreconstructed step edges are shown: zz (zigzag) and ac (armchair). (i) shows a very stable reconstruction of the zz step, consisting of 5- and 7-membered rings. Image source: Phys. Rev. B 99, 115415.

A second important question is whether a portal is more effective when it is entirely clean, or when its edges are decorated with metal atoms. It is well established that metal atoms bind more strongly to vacancy defect sites and step edges than to graphite terraces.[79] For Ru, for instance, the calculated value of E_{ads} is -8.57 eV and -5.42 eV at 1- and 2-atom vacancies on graphene, respectively.[80] A separate study yields a value of -8.15 eV at 1-atom graphene vacancies.[81] Compared to the value of -1.889 eV for adsorption of Ru atoms on graphite *terraces* (Table I), these values are very large.

In fact, for the 1-atom vacancy, E_{ads} of Ru is even higher than the cohesive energy of Ru (Table I). In a case such as this, one could imagine that decoration of the vacancy edge would effectively passivate the step and facilitate passage of other metal atoms over the vacancy edge. However, if edge passivation with metal atoms is necessary, then the minimum size for an active portal could be very large. A simple geometric estimate indicates that m > 6 would be necessary to accommodate two coplanar Cu atoms, for instance.

Analogies with steps. Structures of graphite vacancies and steps are shown in Fig. 12. Steps are often regarded as a type of surface defect. The zigzag (zz) step edge is the most reactive and least stable, while the armchair (ac) step edge is more stable.[77, 82] Both can reconstruct into more stable configurations involving 5- and 7-atom rings. The unreconstructed

zigzag edges, with their cus-C atoms, have partial radical character whereas the armchair edges do not.[82] It is thus natural to expect that the zz steps may be analogous to regions of vacancies with cus-C atoms, and ac steps (or reconstructed step edges) to regions without cus-C atoms.

Han *et al*. undertook a detailed DFT study of intercalation of Cu atoms at the edges of graphite steps, both clean and decorated with a pre-existing chain of Cu atoms.[77] They found that if a clean step is highly reactive, like the zz step, then decoration with Cu atoms passivates the step and facilitates passage of other Cu atoms into the gallery. But the opposite is true if the clean step is less reactive, where decoration with Cu atoms impedes passage. These effects can be deduced from Fig. 13(c) for the zz and ac steps plus a very stable reconstruction labeled zz57, by comparing the positions of the dashed and solid horizontal lines for a given color (given step type), in the region labeled 'Cu atom at step'. This leads to the hypothesis that the optimal configuration of a vacancy is one in which any cus-C atoms are decorated (passivated) during Cu intercalation, while the remaining perimeter of the vacancy is clean. It also suggests that a 6-atom vacancy with the configuration of Fig. 12(f), with many cus-C atoms, would not be very effective despite its large size.

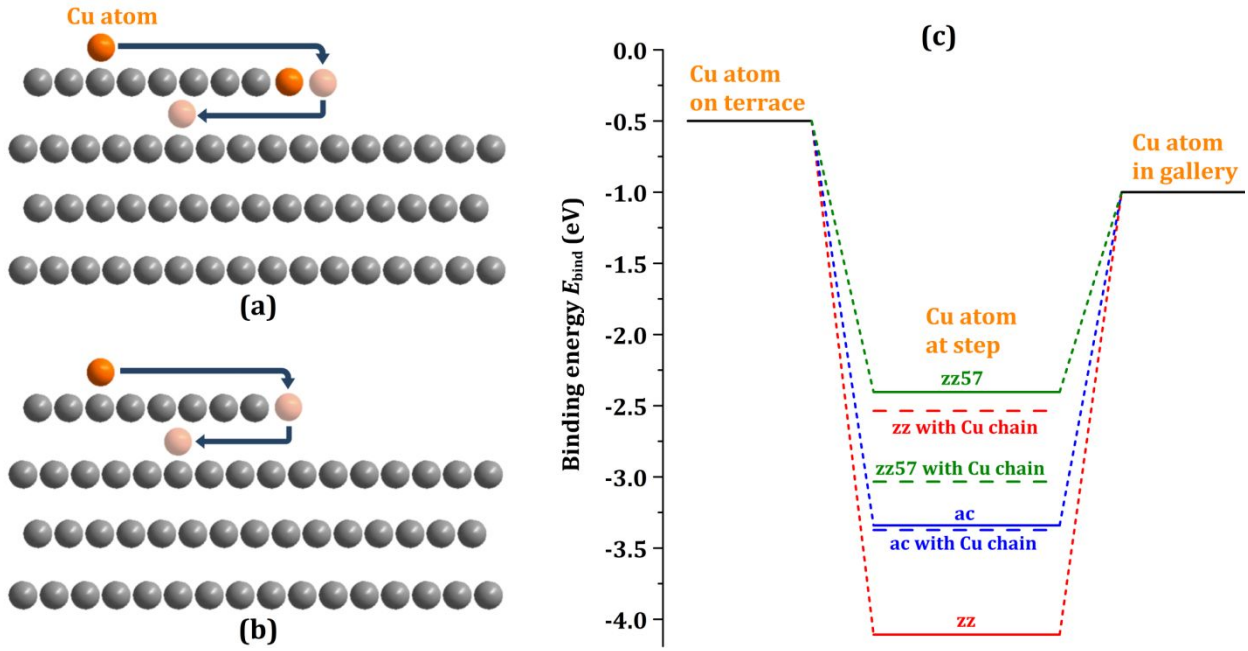

Figure 13. (a, b) Side-view schematics of intercalation path of a single Cu atom. In each view, the atom begins on a graphite terrace, binds at the step, and passes into the gallery. In (a) the step edge is decorated with a chain of Cu atoms, whereas in (b) it is clean. (c) Energy levels corresponding to the paths in (a, b). Image source: Phys. Rev. B 99, 115415.

6. Classes of systems.

Observations. The dimensions and areal densities of ECs, summarized in Table II, span a broad range. At one extreme, there is Ru and Dy,[12, 14] which have small islands and high island densities. In this context, 'small' means that the island heights are only a few atomic layers of metal, and diameters are on the order of 10-20 nm. At the other extreme, there is and Cu and Fe,[13, 15] with large islands and low island densities. Here, 'large' means that heights are ten(s) of atomic layers of metal, and diameters are about 50-80 nm on average. In the middle there is Pt,[16] with small islands (dimensions similar to Ru and Dy) but low densities (comparable to Cu and

Fe). Hence it is natural to place Fe and Cu in one class, and Ru and Dy in another, with Pt in between.

Explanations. A possible explanation for the two classes has been proposed.[15] There is evidence that Fe ECs can diffuse, collide, and merge—a process known as Smoluchowski ripening—during growth.[15] Examples of ECs that appear to be merging are shown in Fig. 14. It may even be that such merging is facilitated by the elastic interactions between two ECs mediated by the graphene membrane, creating, in effect, an attractive interaction between ECs. If Smoluchowski ripening is efficient, it could account for the large EC size and low EC density—both for Fe and Cu. In this picture, Ru and Dy ECs do not diffuse, but rather remain fixed at or near the point of nucleation. It is interesting that in Table I, Ru and Dy have significantly higher values of E_{ads} than do Cu and Fe, which may help explain less facile EC diffusion for Ru and Dy.

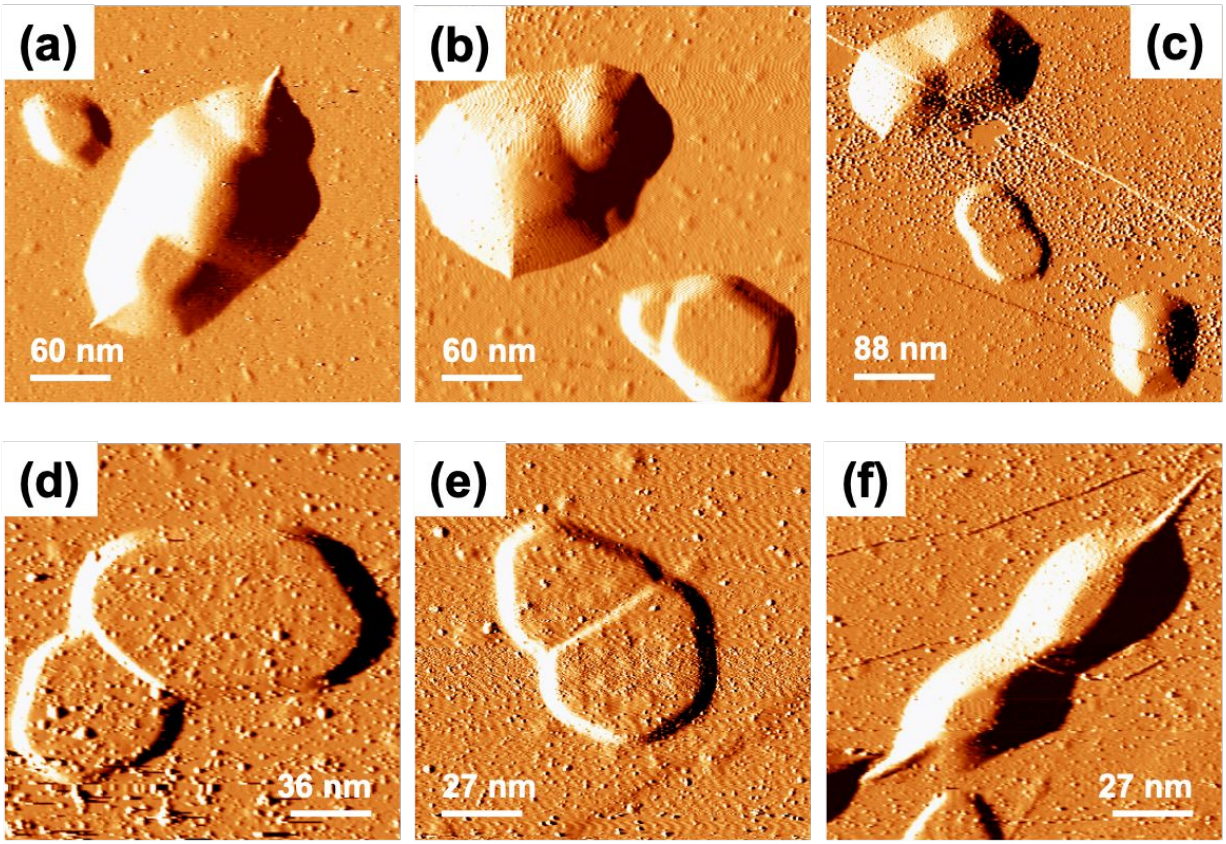

Figure 14. Examples of merged ECs: (a-c) Cu and (d-f) Fe. Small, particle-like features on top of the encapsulated islands and on the substrate are clean defects from ion bombardment, or defects that are decorated with bare metal atoms. Image source: (d, f) Reprinted from A. Lii-Rosales *et al*., Journal of Vacuum Science & Technology A, 37, 061403, (2019), with the permission of AIP Publishing.

That leaves the case of Pt, where a different explanation has emerged.[16] The difference in a Pt atom's chemical potential, between the most favored adsorption site and the most favored intercalated site, $\Delta\mu_M$, is only -0.2 eV. This is small when compared with the other three EC-forming transition metals, for which $\Delta\mu_M$ ranges from -0.5 eV for Cu to -1.2 eV for Fe. (The single-atom energetics, for all of the metals studied to date, are summarized in Table III.) Hence the density of the Pt-atom gas beneath the graphite surface is relatively low, leading to a lower probability for nucleation and growth of ECs. The proposal is thus that the Pt islands are

stationary, like Ru and Dy, which accounts for their small size (no coarsening). However, the density of Pt islands is low, like Cu and Fe, because the probability of nucleation and growth is low.[16]

Table III. Values of $\Delta\mu_M$ in eV for single atoms of different metals.

M	$\Delta\mu_M$, eV	Source
Cu	-0.5	[13]
Fe	-1.2	[15]
Ru	-1.0	[14]
Dy	-0.9	[24]
Pt	-0.2	[16]
Ag	+0.8	[16]
Au	+1.2	[16]

Challenges. There are several other differences and similarities between these metals, in terms of EC characteristics, which are not understood at this time. One is the difference in shapes, illustrated by the line profiles in Fig. 5: Most are flat-topped, but some have round tops. Cu displays both shapes, with round tops dominating for larger Cu ECs; and Pt displays exclusively round tops. Another is the fact that the graphene membrane consists of multiple GMLs on Cu and Fe, but a single GML on Ru. This may be tied to the diffusion of Cu and Fe GMLs, posited above: EC diffusion beneath a step in the up-going direction on the graphite surface would lead to a thicker membrane.

Ramification. Returning to the issue of reaction with carbon, introduced in Sec. 4: The division of metals into (Cu, Fe) and (Ru, Dy) groups does not follow the lines expected if carbon solubility or carbide formation were important factors. In the precipitation-growth scenario for encapsulation, Fe, Ru, and Dy should be similar, but instead, Fe resembles Cu, which has very low affinity for C. This supports the conclusion that carbon does not play a significant role in EC formation.

Summary. To summarize this section, the metals studied to date can be divided into two main groups, with one metal being intermediary. The grouping is based on the EC size and areal density. It can be rationalized on the basis of EC coarsening for one class but not another, plus differences in $\Delta\mu_M$.

7. DFT calculations of stability.

DFT calculations have proven extremely valuable in understanding the role of kinetics versus thermodynamics in encapsulation. First, however, some of the major considerations in setting up the DFT calculations themselves are presented.

Considerations in DFT. The configuration of the metal and the layered material is one of the most important choices. Regarding the metal, at one extreme, one can use a very low coverage of metal—corresponding to a single metal atom in a large lateral supercell—which approaches the single-atom limit. At the other extreme, one can use a dense metallic slab (a.k.a film) consisting of a variable number of layers L_M. Both of these extreme configurations—single metal atom and metallic slab—have been examined in the literature, as well as intermediate configurations.

The choice of supercell for a metal slab is determined by a balance between computational resources available, and the strain introduced by a commensurate supercell

between the bulk metallic lattice and the bulk layered material. For example, for fcc Cu or hcp Fe a simple (1 × 1) supercell (relative to graphene) gives a reasonably small lattice mismatch of -3.9% or +0.244%, respectively (where the negative sign denotes compressive strain),[13, 15] while for Ru a large unit cell of (11 × 11) is needed to produce small lattice mismatch, in this case -0.35%.[14] The computational demands in the former case are obviously much smaller than in the latter case.

The configuration of the layered material is also important, particularly the number of layers used to mimic the bulk-like material, L_{l}. The case $L_{\mathrm{l}} = 4$, which is generally appropriate for graphite, is shown in Fig. 15, with the bottom-most layer frozen and others allowed to relax.

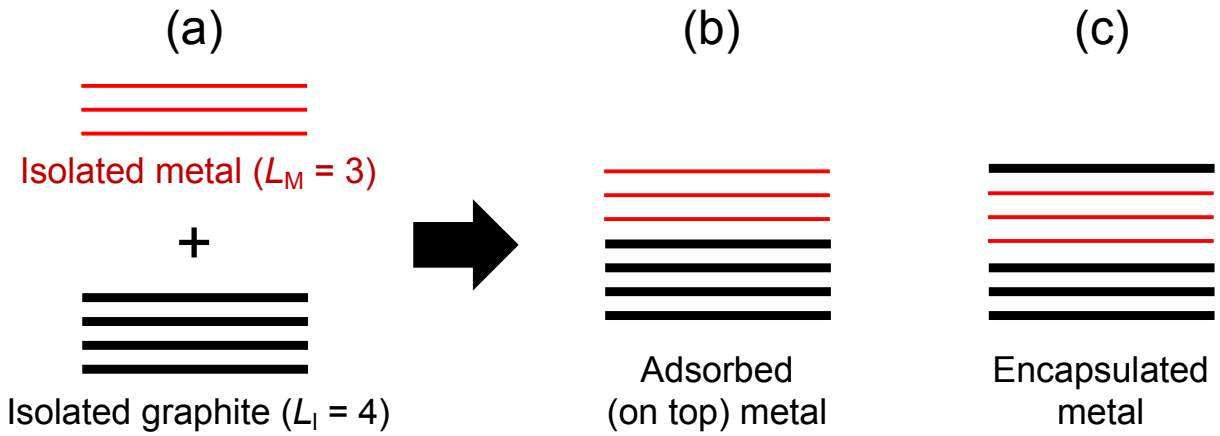

Figure 15. Configurations of a layered material and metal considered in DFT calculations for ECs.

Among the remaining variables in a DFT calculation is the nature of the functional. For a system that incorporates both metal and 2D material, such as Fig. 15(b, c) the best functional is one which gives good benchmark results for both the isolated bulk metal and the isolated 2D material. For this purpose, the optB88-vdW functional is a good choice, because it incorporates the dispersion corrections that are important in the 2D material, but also gives good results for cohesive energies and lattice constants for pure bulk transition metals.[83, 84]

Finally, in DFT, the energetic parameter of interest must be identified. A useful metric is the chemical potential of the metal M (at 0 K), defined as

$$\mu_{\mathrm{M}} = \frac{E_{\mathrm{tot}} - E_{\mathrm{graphite}}}{n} - E_{\mathrm{M}} \qquad (2)$$

where E_{tot} is the total energy of the metal-plus-graphite system, E_{graphite} is the energy of graphite substrate, and E_M is the energy of one metal atom in the gas phase. For one adatom ($n = 1$) adsorbed on the substrate, Eq. (1) reduces to the conventional expression for adsorption energy, $E_{\mathrm{ads}} = E_{\mathrm{tot}} - E_{\mathrm{graphite}} - E_{\mathrm{M}}$.

Results from DFT slab calculations. Key results from slab calculations are shown in Fig. 16 for Cu, Ru and Fe, where μ_{M} is plotted as a function of L_{M}. For Fe, the isolated (i.e., freestanding) slab has the highest (least favorable) μ_{M} and the encapsulated slab (covered by a single layer of graphene) has the lowest, with the adsorbed slab being intermediate. Hence, encapsulation is favored over adsorption. These differences are especially notable at small L_{M}.

As L_M increases, all values converge toward the bulk cohesive energy of the metal, because the relative importance of the surrounding layered material diminishes. For Ru the differences between the adsorbed and encapsulated phases are less pronounced, and for Cu, there is no indication that the encapsulated phase is favored at any L_M; μ_M of the adsorbed and encapsulated phases are essentially equal even at low L_M. This brings into question the thermodynamic driving force for encapsulation, at least for Cu.

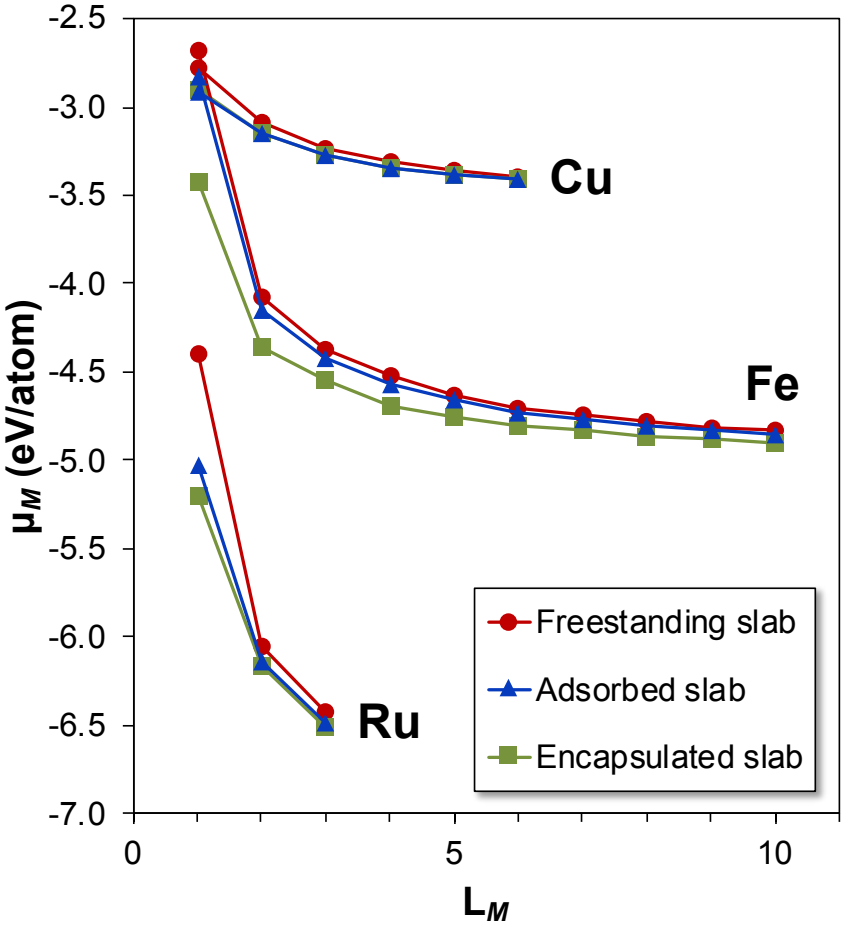

Figure 16. Chemical potential as a function of the number of metal layers, for 3 metals (Cu, Fe, Ru) and 3 slab configurations of each metal (freestanding, adsorbed, and encapsulated). For Cu, the curves for encapsulated and adsorbed slabs overlap.

Results from DFT cluster calculations. The conundrum described above is resolved by examining single atoms and small clusters, rather than slabs. Results for Cu are shown in Fig. 17. It can be seen that encapsulation of the small clusters is strongly *unfavorable* for all clusters (n > 1), but it is strongly *favorable* for the single atom (n = 1). This suggests that the density of single atoms is much higher in the galleries than on top of the surface, assuming that the portals facilitate a quasi-equilibrium between adsorbed and intercalated atoms during deposition. This leads, in turn, to a hypothesis that the single atoms in the galleries nucleate into islands, which then are trapped in the galleries. In other words, growth of encapsulated islands is driven by kinetics rather than thermodynamics. For metals other than Cu, where slab calculations indicate that intercalation is favored (Fig. 16), both factors may play a role.

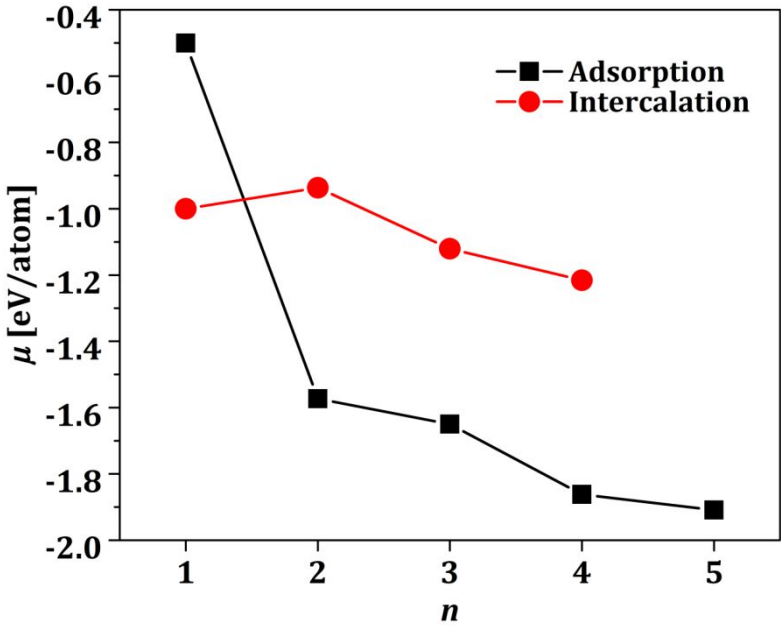

Figure 17. Chemical potential μ as a function of the number of Cu atoms, n, in a cluster ($n > 1$), or as a single atom ($n = 1$). The red dots show results for intercalated clusters/atoms, while the black squares show results for adsorbed clusters/atoms. Image reprinted with permission from J. Phys. Chem. C, 2018, 122, 8, 4454-4469. Copyright 2018 American Chemical Society.

In the foregoing discussion, the key comparison is between the values of μ_M for intercalated and adsorbed phases, i.e., $\Delta\mu_M$. Occasionally, in judging whether intercalation is favorable, the comparison is made between μ for the intercalated phase and for the isolated species (isolated atom, or isolated slab).[15, 85] However, the isolated species is a less physically-informative reference point, because the mechanism of encapsulation is a stepwise process involving adsorption of metal from the gas phase, followed by encapsulation. This is clear from our experimental studies, which consistently show that if T_{dep} is not sufficiently high, the process stops after the first step (adsorption and clustering) and never proceeds to encapsulation. Therefore, a comparison of energetics between the adsorbed phase and the encapsulated phase is most appropriate to determine whether encapsulation is energetically favored.

8. Predicting encapsulation.

Recent experiments have shown that Ag and Au do not form ECs.[16] This is consistent with DFT results, which show that single atoms of Ag and Au are less favored in the galleries than atop the surface.[16] In fact, they are disfavored by large amounts, 0.8 eV and 1.2 eV, respectively (Table III). Additional DFT investigations reveal a correlation between the metal's Shannon effective ionic radius and $\Delta\mu_M$, where adsorption is favored over intercalation for metal atoms above a critical Shannon radius (0.1 nm).[24] Both Ag and Au have a Shannon radius above 0.1 nm, consistent with experimental observation of no EC formation. For each of the other transition metals Cu, Fe, Ru, and Pt, the Shannon radius is below 0.1 nm, and single-metal-atom energetics favor encapsulation.

This result supports the validity of using single-metal-atom energetics to predict encapsulation at the graphite surface. This is important, because calculations involving single metal atoms are generally simpler and less expensive than calculations involving metal clusters

or metal slabs at least for cases where a large unit cell is needed to produce a small lattice mismatch (plus graphite).

9. Kinetic modeling.

The treatment of conventional nucleation and growth of nanoclusters or islands during deposition on top of surfaces has a long history from Zinsmeister-Venables mean-field treatments initiated in the late 1960's[86, 87] to more precise beyond-mean-field treatments developed into the 2000's.[88] However, the complex process of competitive nucleation and growth of nanoclusters on top of the surface versus intercalated or encapsulated in galleries has not been considered previously. From this perspective, it is natural to start with a simplified analysis of just one key component of this overall process: nucleation and growth of intercalated islands within the galleries fed by a prescribed flux of atoms through defect portals.[89] This simplified modeling still yields valuable insights.

In this simplified stochastic lattice-gas modeling targeting formation of ECs, defect portals are considered to be well-separated so that island nucleation nearby each portal can be considered independent of this process at other portals.[89] Then, the key components of the model include: injection of atoms into the gallery through the isolated portal with a prescribed flux; diffusion of atoms within the gallery; and aggregation of these diffusing atoms into clusters reflecting attractive interactions between adatoms. The shapes of growing islands are controlled by rates for periphery diffusion of aggregated atoms which must also be specified consistent with the adatom interactions. The stochastic model is illustrated in Fig. 18.[89] Note that the injection flux implicitly reflects multiple factors: the "capture zone" area for the portal defect which is the region of the surface for which deposited atoms are most likely to reach the defect; the ease of nucleation of islands on top of the surface (as such nucleation reduces the flux into the gallery); and the presence of any energetic barrier for atoms to transit the portal into the gallery.

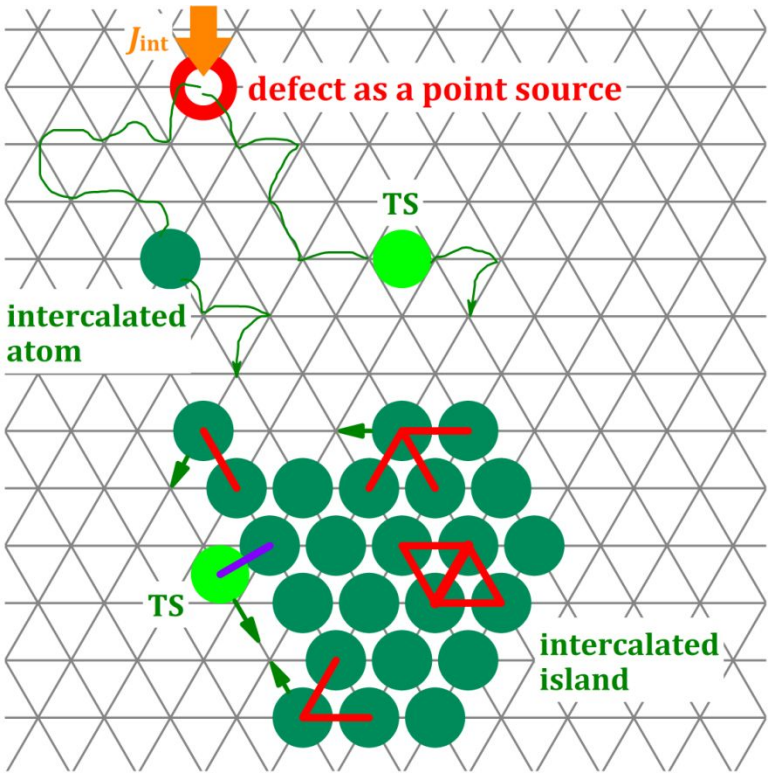

Figure 18. A schematic of the stochastic model with defects as point sources for entry into the gallery below the top layer. Image source: Phys. Rev. Mater. 1, 053403, 2017.

For this stochastic model involving a single point defect portal, precise behavior is obtained from Kinetic Monte Carlo (KMC) simulation using a triangular lattice to reflect adatom adsorption sites in the gallery, a choice consistent with the structure of graphene layers, and also with the expected hexagonal close-packed layers and the observed footprint shapes of ECs. Basic features of the nucleation process, as characterized by KMC simulation, can be elucidated by an analytic treatment. The latter involves solving the continuum 2D diffusion equation with a localized delta function like injection term for the spatiotemporal evolution of the density of injected atoms within the gallery prior to nucleation.[89]

One might intuitively suspect that encapsulated islands develop directly below entry portals. The modeling showed that this expectation is, however, too simplistic.[89] The reason can be understood within the context of Fig. 19. The top panel shows the nucleation probability per site (or per unit area) as a function of scaled radial distance, $r/\langle r_{nuc}\rangle$, from the portal, where $\langle r_{nuc}\rangle$ denotes the mean nucleation distance from the portal. Indeed, this probability peaks directly beneath the portal at $r = 0$. However, the bottom panel shows that the probability of nucleation within an increment of distance r to $r + dr$ from the portal reaches a maximum at a finite distance $\langle r_{nuc}\rangle$ away from the portal. This is because the number of sites per increment of radial distance, dr, increases linearly with r. The physical implication is that nucleation tends to occur some distance from the portal, counter to expectation.

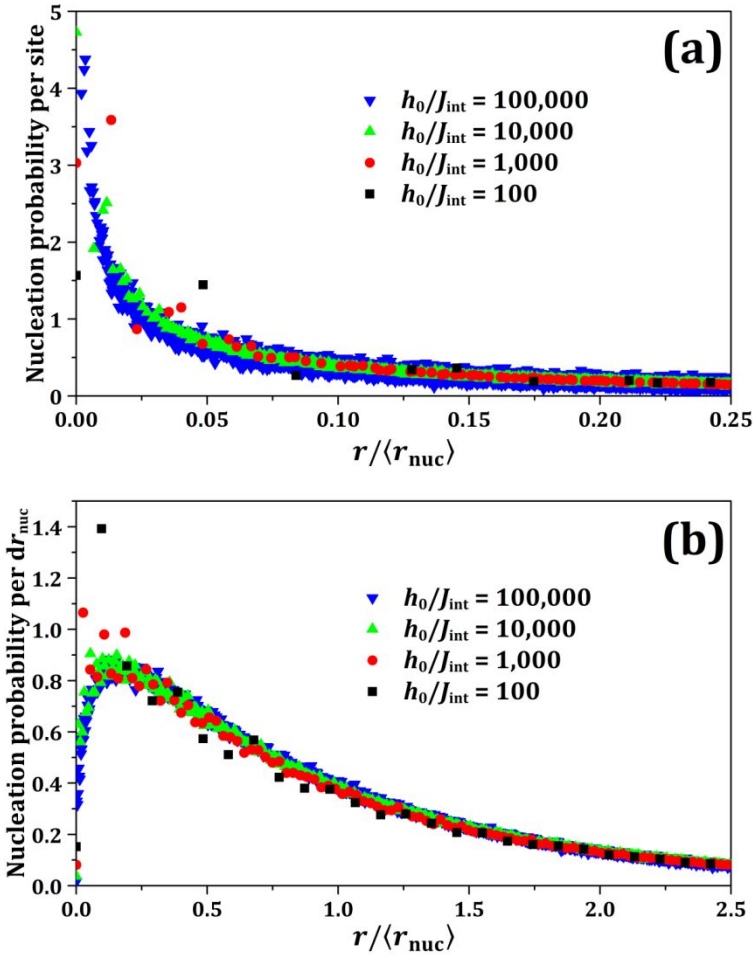

Figure 19. Nucleation probabilities (a) per site, and (b) per unit area. The x-axis is the scaled radial distance from the point-source portal (r = 0 is the portal location). Curves are shown for various values of h_0/J_{int}, where h_0 is the hop rate and J_{int} is the rate at which atoms pass through the point source. The critical island size is set to i = 1. Image source: Phys. Rev. Mater. 1, 053403, 2017.

Furthermore, KMC simulation shows that ECs tend to grow back towards the portal. If nucleated sufficiently close to the portal, the EC will eventually touch it, thereby blocking the portal. (Many islands nucleate too far from the portal for this blockage to occur.) This is illustrated in Fig. 20, which also includes experimental STM data for Dy for comparison. It can be seen that the encapsulated Dy islands often have an appended cluster at their upper edge. Presumably these clusters grow above an entry portal when it becomes blocked by the underlying Dy, which is entirely consistent with the modeling. However, this type of configuration is not seen for other metals, which may be due to cluster diffusion away from entry portals or a higher probability for nucleation far from portals.

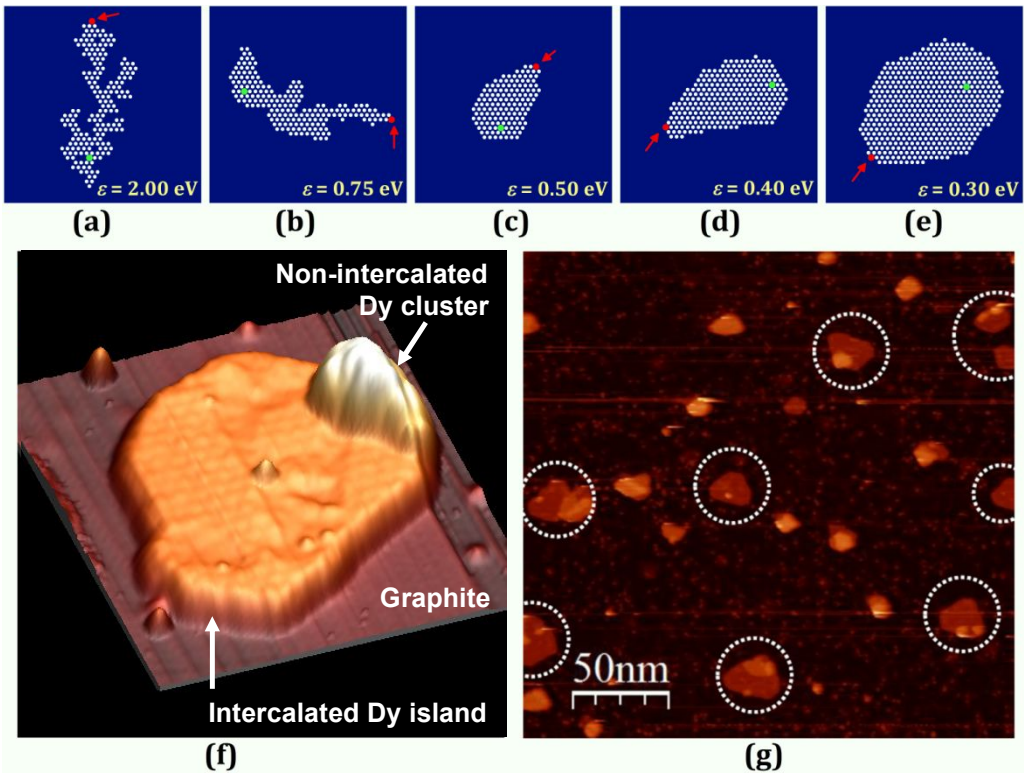

Figure 20. (a-e) Examples of nucleated islands from Kinetic Monte Carlo simulations with $h_0/J_{int} = 4000$. The parameter ε is the short-range pairwise interaction energy between intercalating atoms, corresponding to the short red linear segments in Fig. 18. From left to right, ε varies from 2.00 eV to 0.30 eV. Critical size i also varies from $i = 1$ in (a) to $i > 1$ in the other panels. The small red dot, indicated by a red arrow, shows the point source location. The large green dot shows the approximate point of nucleation. (f) STM image of a single Dy island, showing an appended cluster at the edge of an encapsulated island. (g) Lower-magnification STM image showing many encapsulated Dy islands (encircled), each with an appended cluster (brightest feature) at the edge. Image source: Phys. Rev. Mater. 1, 053403, 2017.

Another insight from KMC simulation relates to the shapes of the growing ECs. In experiment, they are typically compact and faceted (Fig. 20(f-g)). The modeling includes an effective pairwise interaction energy between adatoms, ε. If ε is too high relative to the thermal energy, then aggregation is irreversible, periphery diffusion is strongly inhibited, and ECs are fractal-like as in Fig. 20(a-b). Experiment for Dy appears to correspond to lower values of ε as in Fig. 20(c-d), where aggregation is reversible and periphery diffusion more facile although island shapes are not fully equilibrated.

A future challenge is to develop a more complete and realistic stochastic model, one that addresses the overall process of competitive formation of clusters on the surface and in the gallery for a surface with multiple defect portals. Work is underway and details will be reported elsewhere.[90] Given the complexity of the process, it is convenient to utilize a so-called point island model which tracks only island size but not structure,[91, 92] but which nonetheless can capture the above mentioned competition. Of course, now the model must treat atom diffusion and aggregation on the surface as well as in the gallery, and explicitly treat transport through the portal. However, a key additional parameter is the binding of metal atoms in clusters as a function of size, a parameter that controls the rate of atom detachment. A basic feature of the process is that at lower temperatures, atoms become irreversibly captured by clusters/islands on the surface. However, at higher temperatures atomic detachment from surface islands is facile, as

is transport of atoms through portals to the gallery to form ECs. This behavior is consistent with experimental observations, e.g., for Cu ECs.

10. Factors governing shapes of the nanoparticles.

Aspect ratio, *d*/*h*. One of the most intriguing aspects of the ECs is their flatness, as reflected in a high aspect ratio *d*/*h*, where *d* is the diameter and *h* is the height. (Fig. 7 represents the presumed shape of a flat-topped EC and defines key dimensions.) As noted in Sec. 1, high aspect ratio implies a high surface-to-volume ratio and an extended area of contact with the 2D material. Many applications of solid metals—as catalysts, magnets, sensors, heat sinks, or electrodes, to name a few—are most efficient and cost-effective when the surface-to-volume ratio of the metal is high.

Fig. 21 shows the aspect ratio as a function of *h*, for the two metals that exhibit the largest ECs, Cu and Fe.[10, 11] Modeling the shapes of these ECs has been carried out using continuum elasticity (CE) theory, which assumes the metal ECs have a cylindrical shape (a simplification as the true shape is facetted) and are shape-equilibrated.[10, 11] The elastic response of the graphene membrane was treated within the shaft loaded blister test (SLBT) model.[93] Basically, the growing EC pushes upward against the membrane but the layered material resists deformation, thereby forcing the metal cluster between the layers to adopt a much flatter profile (higher aspect ratio) than it would otherwise.[10, 11] This was put on a quantitative basis by comparing the measured *d*/*a* values (in the limit of large *h*) with those for equilibrated clusters supported on a graphite substrate, but *without* the top membrane. The measured aspect ratio of the ECs is higher by about a factor of 10 for Cu, and 5 for Fe.[10, 11]

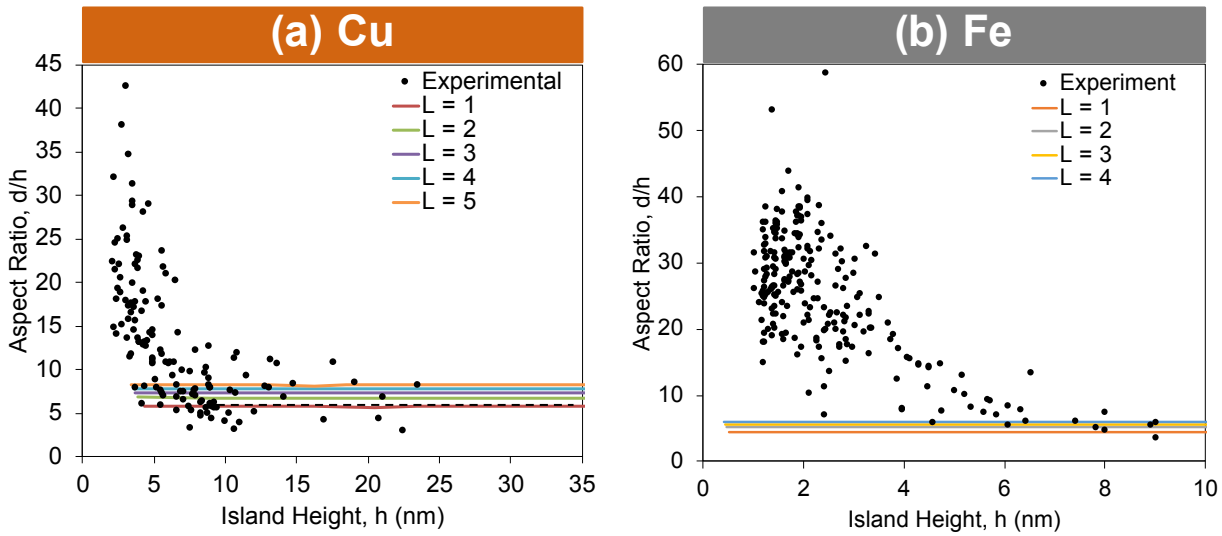

Figure 21. Aspect ratio *d*/*h* as a function of h for (a) Cu ECs and (b) Fe ECs. Image source: (a) Nanoscale, 2019, 11, 6445-6452 - Published by The Royal Society of Chemistry. (b) Ann Lii-Rosales *et al*. 2020 New J. Phys. 22 023016.

The model included only one adjustable parameter, L_l, the number of GMLs in the membrane. Inputs to the model included surface and interfacial energies corresponding to the surface and interfaces shown in Fig. 7. These energies were calculated with DFT. Physical parameters, such as Young's modulus of graphene, were obtained from the literature.

The horizontal lines in Fig. 21 show the results of modeling for different values of L_l. The model produces a good quantitative fit for large values of *h*, but fails for small *h*: the aspect ratio

of small clusters is much higher than predicted. Several possible explanations for this discrepancy were considered, among them the fact that the model did not allow coupled stretching and bending of the membrane; the possibility that atomistic effects invalidate some of the surface and interfacial energies at small *h*; and deformation of the underlying graphite surface. None of these factors proved viable, so the discrepancy remains unexplained within the context of an equilibrium model. One remaining possibility is that the aspect ratios of the small islands are influenced strongly by kinetic factors, whereas the larger islands are less influenced, though this would contradict expectation. In short, understanding the steep rise in d/h at small h remains an open challenge.

Annulus slope, h/a. The slope of the graphene blanket constituting the sides of the islands, h/a, also contains information. As shown in Fig. 7, the volume beneath the sloping sides is believed to be empty. This follows, in part, from the frequent presence of wrinkles at the corners of the annulus. Examples are visible in Fig. 5(e) and Fig. 14(a, f). These wrinkles suggest that there is no underlying material or support that would restrict the membrane from folding. Also, the slope of the annulus is shallow and incompatible with any low-index planes of the metal (assuming that the top and bottom facets are close-packed planes), so any underlying support would have to consist of energetically-costly high-index planes.[10]

The value of h varies linearly with a over the entire range of h, as shown in Fig. 22(a, c), for both Cu and Fe ECs. Another representation, h/a vs. h, is given in Fig. 22(b, d). Both representations show that the slope h/a is a constant, independent of h. Again, the horizontal lines in Fig. 22(b, d) show the results of modeling for different values of L_l. There is excellent agreement between theory and experiment. Optimal values of L_l are 3-4 for Cu and 2-3 for Fe.[10, 11]

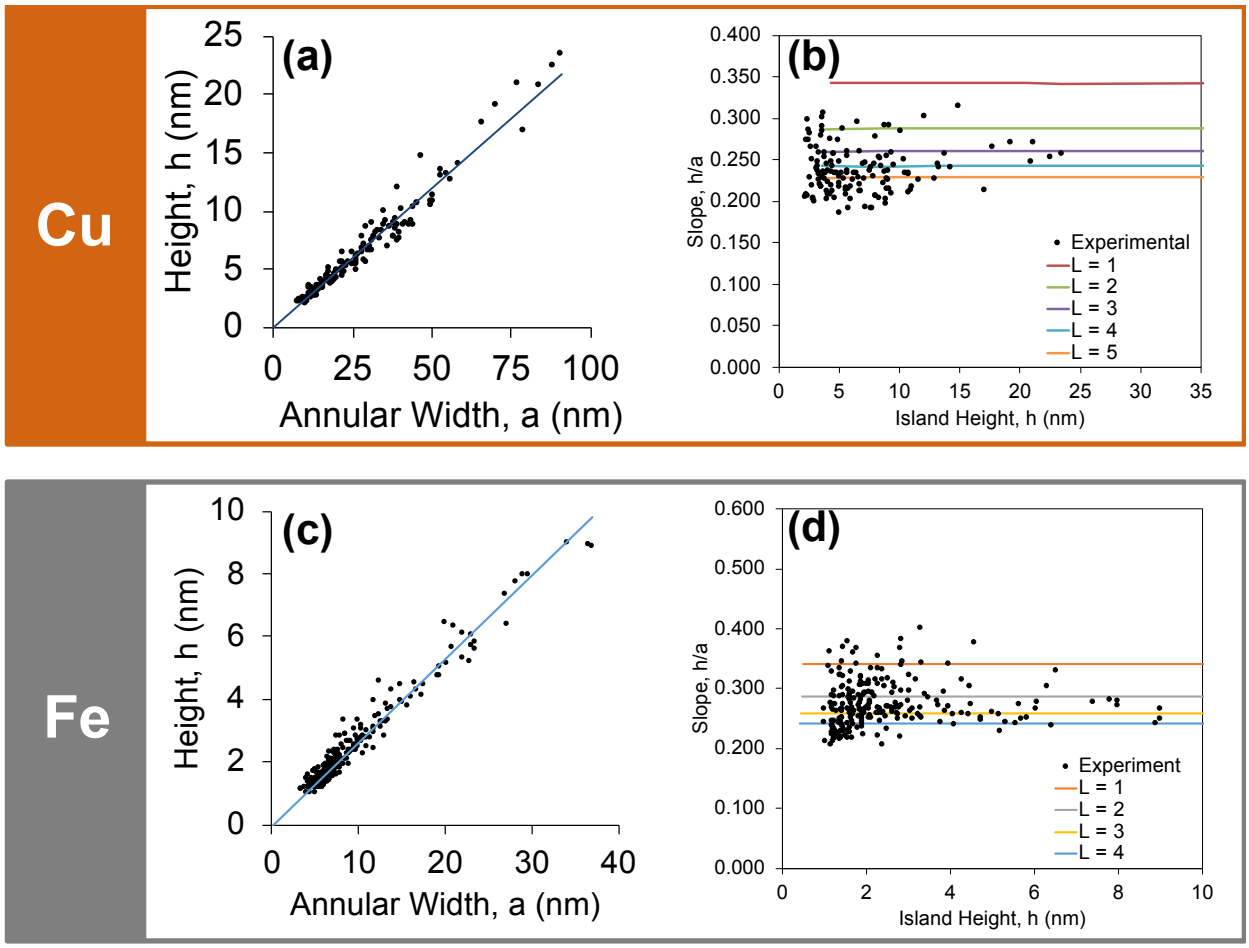

Figure 22. Height (h), annular width (a), and annulus slope (h/a) for Cu and Fe ECs. Image sources: (a, b) Nanoscale, 2019, 11, 6445-6452 - Published by The Royal Society of Chemistry. (c, d) Ann Lii-Rosales *et al*. 2020 New J. Phys. 22, 023016.

The physical interpretation of this constant slope is as follows. Delamination in the annulus is purely a response to the upward displacement, *h*, of the membrane at the inner circumference of the annulus. As such, *a* depends on the mechanical properties of the graphene membrane and its adhesion to the graphite substrate—and does not depend on the nature of the metal or the metal cluster's diameter. This conclusion is reinforced by the similar values of *h*/*a* for Cu and Fe in Fig. 22. Given this insight, it is possible to apply simpler models to predict the value of *h*/*a*, which may prove useful for other layered materials.[11]

Universal shape. Interestingly, the constancy of *d*/*h* and *h*/*a,* corresponding to horizontal lines in Fig. 21 and Fig. 22, means that the model predicts a size-invariant shape (profile) of the EC. This was rationalized by analysis of the individual energy terms that control the shape of the EC.[10, 11] This is reminiscent of the equilibrium crystal shape of a free or supported solid crystalline particle, which is also size-invariant.

True facetted shape of the metallic component of the EC. As noted above, given the complexity of the analysis of the strain component of the energy of the system in the above continuum elasticity modeling, a simplification was made treating the metallic nanocluster as having cylindrical shape. However, the actual shape is expected to be facetted, and has been recently determined by a suitable refinement of the Winterbottom construction for supported

nanoclusters (which itself is a refinement of the Wulff construction for unsupported clusters).[94] An example of such a facetted shape for encapsulated Cu is shown in Fig. 23.

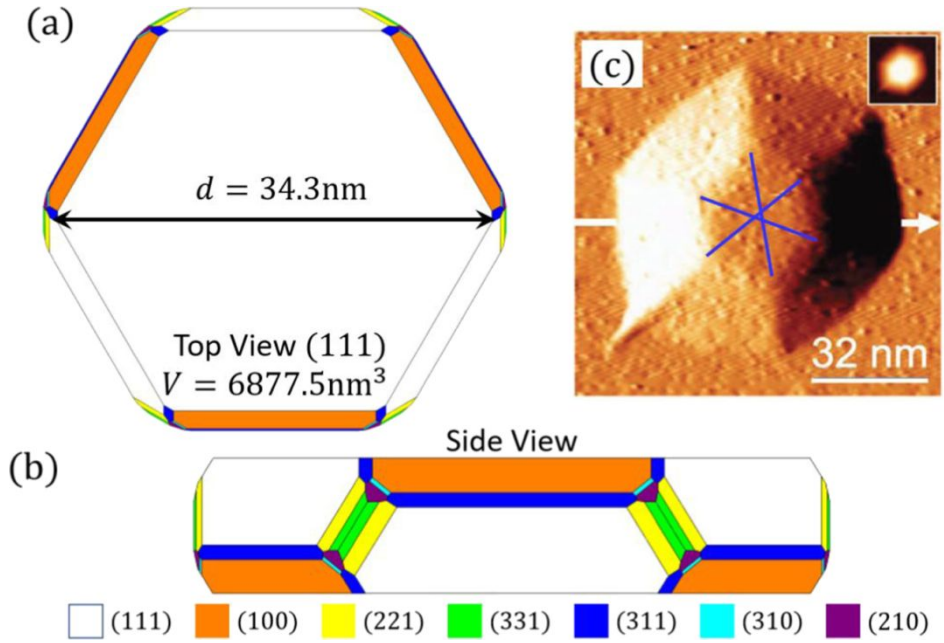

Figure 23. The equilibrium shape of the metallic fcc Cu component of an EC with the experimental height of 7.83 nm and diameter $d \approx 34.3$nm obtained from numerical energy minimization. Views are shown: (a) orthogonal to the substrate, and perpendicular to (111) top and bottom facets; and (b) from a horizontal direction. Various surface facets present are indicated. Corresponding derivative-mode experimental image with the same height and diameter is shown in (c). Image source: J. Phys. Condens. Matter 32 (2020) 445001.

Summary. To summarize this section, the vertical profile of an EC can be described by its aspect ratio d/h, together with its side slope, h/a. CE modeling successfully captures the former in the limit of large islands, and the latter in the entire range of island sizes. The aspect ratio is quite large, due to the graphene membrane's resistance to distortion. The side slope is determined solely by the delamination of the membrane in response to the upward pressure exerted by the cluster. For a given metal, the equilibrated ECs have a size-independent shape that is analogous to an equilibrium crystal shape.

11. Stability in air.

As noted in Sec. 1, one of the potential advantages of encapsulation is to protect the encapsulated metal from oxidation. This possibility has been tested under relatively mild conditions, by exposing ECs to air at room temperature.

Fig. 24 shows the results for Fe,[15] which is similar to results for Cu and Ru. In each case, the sample with freshly prepared ECs was characterized with XPS and STM in UHV. The ECs are clearly visible in Fig. 24(a), and the top XPS spectrum in Fig. 24(c) is that expected for metallic Fe. The sample was then removed from UHV, exposed to air, and returned to the UHV chamber where it was characterized with XPS. The middle XPS spectrum in Fig. 24(c) shows that some of the metal has oxidized, and this is corroborated by the O 1*s* spectrum in Fig. 24(d). Following this the sample was outgassed. At this point the ECs were characterized in STM (Fig.

24(b)), and XPS (bottom spectrum in Fig. 24(c)) indicated that the metal had mostly returned to the metallic state.

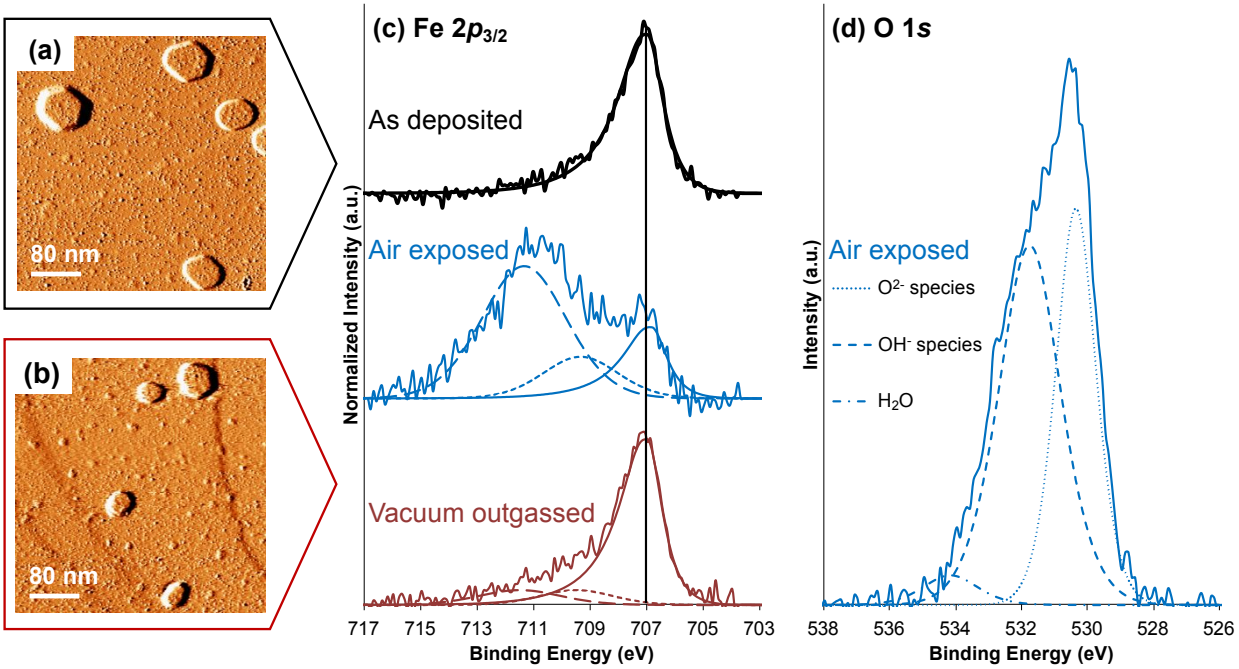

Figure 24. Fe ECs (a) as-prepared and (b) after vacuum outgassing. (c, d) XPS of Fe $2p_{3/2}$ and O 1*s* of Fe ECs at various preparation stages. Image source: (c, d) Reprinted from A. Lii-Rosales *et al*., Journal of Vacuum Science & Technology A, 37, 061403, (2019), with the permission of AIP Publishing.

The interpretation of these data, and similar data for Cu and Ru, was that the Fe ECs were protected during air exposure.[15] Oxidation took place at a different type of Fe, i.e., very small adsorbed Fe clusters pinned at defect sites. These small clusters, or their oxides, formed first during air exposure. They largely prevented oxygen from penetrating the portals and attacking the ECs. Upon outgassing, the oxide was removed at these sites. Thus, the graphene membrane—though highly defective—can protect transition metal ECs from air oxidation, at least at 300 K.

It is noteworthy that Dy is an exception. There is strong evidence that Dy ECs oxidize upon air exposure, even though the overlying graphene membrane remains intact.[17] A possible cause for oxidation is the bare, appended Dy cluster on top of the Dy ECs. Examples are shown in Fig. 20(f, g). The bare Dy cluster can oxidize in air, from where oxidation can propagate to the encapsulated Dy. Data are not available for Pt but presumably resemble the other late transition metals.

12. Conclusions.

As indicated above, the near-surface intercalation of metallic nanoclusters in the layered material, graphite, is a recent experimental discovery. This should be contrasted with extensive experimental studies for more than five decades of metallic nanoclusters formed during deposition on top of surfaces. Thus, there remain many questions and opportunities for further experimental analysis of the intercalation systems. On the theoretical side, analysis of the nucleation and growth of metal nanoclusters on top of surfaces is well developed. Such studies

were initiated in the 1960's with mean-field rate equation modeling and have continued through recent years with beyond-mean-field analytic theory and KMC simulation. However, for nucleation and growth of ECs, theory and simulation are currently limited, so again there is great opportunity to develop appropriate predictive theory for deeper understanding of these novel systems.

Another fundamental question is which metals can form ECs. We have described their formation for transition metals Cu, Fe, Ru, and Pt, and the rare earths Dy and Gd. Additional experiments reveal that Ag and Au do not intercalate.[16] Some understanding of the preference for various metal to intercalate or not has been obtained from DFT analysis which compares the Shannon ionic radius of the metal with the size of the gap between graphene layers in graphite. Metals with smaller radii more readily intercalate.[24]

There are opportunities to exploit ECs in applications, as well as to answer unresolved basic questions (as already indicated above).

One natural question is whether the techniques utilized to form ECs on graphite can be employed with other layered materials, such as transition metal dichalcogenides (TMDs), either in bulk or few-layer form. Compared with graphite, it could be more challenging to create appropriate defects in a material such as a TMD, given the multi-atom nature of the top layer in the TMD. Also, it would be very interesting to explore the application of these techniques to few-layer graphene, e.g., bilayer graphene on SiC, to determine whether ECs can be formed. A positive result would be a new development, since to our knowledge, intercalation of metals in few-layer supported graphene involves only a single layer of metal, not the multilayer metallic structures exhibited by ECs.

In Sec. 1, it was mentioned that ECs are good candidates for applications such as heat sinks or electrodes involving 2D or layered materials. This would require spatial control over the entry portals, which should be possible with patterning by using focused ion beams. The ability to pattern ECs is thus an exciting challenge.

Another possible application would be as nanomagnets or even exchange spring magnets. In the latter case, a hard magnetic material such as Dy is in close contact with, and imparts magnetic properties to, a softer magnet. The use of graphene as a barrier between the two metals would impart a degree of structural and chemical integrity that is often difficult to achieve, plus the high aspect ratio of the hard magnetic EC would maximize its efficiency of use.

It would be interesting to determine whether the defects present on the graphite surface after EC formation can be 'healed', for instance by deposition of free carbon. This could bolster the degree of protection afforded to the underlying ECs.

Several basic questions remain unresolved. The high values of aspect ratio for small islands (Fig. 21) are unexplained. The evidence for diffusion and coalescence of some ECs is indirect, but direct confirmation would be desirable. The reason for the existence of round tops for some types of ECs, e.g., for very large Cu islands, and flat tops for others, is unknown. These and other issues are open challenges.

Acknowledgements.

This work was supported by the U.S. Department of Energy (DOE), Office of Science, Basic Energy Sciences, primarily through the Materials Sciences and Engineering Division. The experimental work was performed or supervised by ALR, DJ, MCT, and PAT. DFT calculations were performed by YH, mainly using a grant of computer time at the National Energy Research Scientific Computing Centre (NERSC). NERSC is a DOE Office of Science User Facility

supported by the Office of Science of the U.S. DOE under Contract No. DE-AC02-05CH11231. The calculations also partly used the Extreme Science and Engineering Discovery Environment (XSEDE), which is supported by the National Science Foundation under Grant No. ACI-1548562. KCL and JWE were supported for theory and model development through the USDOE Office of Science, Basic Energy Sciences, Chemical Sciences, Geosciences, and Biological Sciences Division. The research was performed at the Ames Laboratory, which is operated by Iowa State University under contract No. DE-AC02-07CH11358.

References

1. A. H. Castro Neto, F. Guinea, N. M. R. Peres, K. S. Novoselov and A. K. Geim, *Rev. Mod. Phys.*, 2009, **81**, 109-162.
2. W. Han, R. K. Kawakami, M. Gmitra and J. Fabian, *Nat. Nanotechnol.*, 2014, **9**, 794-807.
3. J. Y. Wan, S. D. Lacey, J. Q. Dai, W. Z. Bao, M. S. Fuhrer and L. B. Hu, *Chemical Society Reviews*, 2016, **45**, 6742-6765.
4. J. Hass, W. A. de Heer and E. H. Conrad, *J. Phys. Condens. Matter*, 2008, **20**, 323202.
5. Y. Cao, V. Fatemi, S. Fang, K. Watanabe, T. Taniguchi, E. Kaxiras and P. Jarillo-Herrero, *Nature*, 2018, **556**, 43-50.
6. Q. Fu and X. H. Bao, *Chem. Soc. Rev.*, 2017, **46**, 1842-1874.
7. Y. Wang, J. Mao, X. G. Meng, L. Yu, D. H. Deng and X. H. Bao, *Chem. Rev.*, 2019, **119**, 1806-1854.
8. P. Gargiani, R. Cuadrado, H. B. Vasili, M. Pruneda and M. Valvidares, *Nat. Commun.*, 2017, **8**, 699.
9. V. G. Kravets, R. Jalil, Y. J. Kim, D. Ansell, D. E. Aznakayeva, B. Thackray, L. Britnell, B. D. Belle, F. Withers, I. P. Radko, Z. Han, S. I. Bozhevolnyi, K. S. Novoselov, A. K. Geim and A. N. Grigorenko, *Sci. Rep.*, 2014, **4**, 5517.
10. S. E. Julien, A. Lii-Rosales, K.-T. Wan, Y. Han, M. C. Tringides, J. W. Evans and P. A. Thiel, *Nanoscale*, 2019, **11**, 6445-6452.
11. A. Lii-Rosales, Y. Han, S. E. Julien, O. Pierre-Louis, D. Jing, K.-T. Wan, M. C. Tringides, J. W. Evans and P. A. Thiel, *New J. Phys.*, 2020, **22**, 023016.
12. Y. Zhou, A. Lii-Rosales, M. Kim, M. Wallingford, D. Jing, M. C. Tringides, C.-Z. Wang and P. A. Thiel, *Carbon*, 2018, **127**, 305-311.
13. A. Lii-Rosales, Y. Han, J. W. Evans, D. Jing, Y. Zhou, M. C. Tringides, M. Kim, C. Z. Wang and P. A. Thiel, *J. Phys. Chem. C*, 2018, **122**, 4454-4469.
14. A. Lii-Rosales, Y. Han, K. M. Yu, D. Jing, N. Anderson, D. Vaknin, M. C. Tringides, J. W. Evans, M. S. Altman and P. A. Thiel, *Nanotechnology*, 2018, **29**, 505601.
15. A. Lii-Rosales, Y. Han, K. C. Lai, D. Jing, M. C. Tringides, J. W. Evans and P. A. Thiel, *J. Vac. Sci. Technol. A*, 2019, **37**, 061403.
16. A. Lii-Rosales, Y. Han, D. P. Jing, M. C. Tringides and P. A. Thiel, *Phys. Rev. Res.*, 2020, **2**, 033175.
17. A. Lii-Rosales, Ph.D. Ph.D. Thesis, Iowa State University, 2019.
18. M. S. Dresselhaus and G. Dresselhaus, *Adv. Phys.*, 2002, **51**, 1-186.
19. D. D. L. Chung, *J. Mater. Sci.*, 2002, **37**, 1475.
20. X. Liu, Y. Han, J. W. Evans, A. K. Engstfeld, R. J. Behm, M. C. Tringides, M. Hupalo, H.-Q. Lin, L. Huang, K.-M. Ho, D. Appy, P. A. Thiel and C.-Z. Wang, *Prog. Surf. Sci.*, 2015, **90**, 397-443.

21. X. Liu, M. Hupalo, C.-Z. Wang, W.-C. Lu, P. A. Thiel, K.-M. Ho and M. Tringides, *Phys. Rev. B*, 2012, **86**, 081414(R).
22. X. Liu, C.-Z. Wang, M. Hupalo, H.-Q. Lin, K.-M. Ho and M. C. Tringides, *Crystals*, 2013, **3**, 79-111.
23. X. Liu, C. Z. Wang, M. Hupalo, W. C. Lu, M. C. Tringides, Y. X. Yao and K. M. Ho, *Phys. Chem. Chem. Phys.*, 2012, **14**, 9157-9166.
24. W. Li, L. Huang, M. C. Tringides, J. W. Evans and Y. Han, *J. Phys. Chem. Lett.*, 2020, **11**, 9725-9730.
25. C. Kittel, *Introduction to Solid State Physics*, John Wiley & Sons, Inc., Hoboken, NJ, 2005.
26. E. J. Kwolek, H. Lei, A. Lii-Rosales, M. Wallingford, Y. Zhou, C.-Z. Wang, M. C. Tringides, J. W. Evans and P. A. Thiel, *J. Chem. Phys.*, 2016, **145**, 211902.
27. D. Appy, H. Lei, Y. Han, C.-Z. Wang, M. C. Tringides, D. Shao, E. J. Kwolek, J. W. Evans and P. A. Thiel, *Phys. Rev. B*, 2014, **90**, 195406.
28. R. W. G. Wyckoff, *Crystal Structures*, Interscience, New York, 1963.
29. F. Atamny, O. Spillecke and R. Schlögl, *Phys. Chem. Chem. Phys.*, 1999, **1**, 4113.
30. J. L. Paredes, A. Martinez-Alonso and J. M. D. Tascon, *Carbon*, 2001, **39**, 476-479.
31. S. Hembacher, F. J. Giessibl, J. Mannhart and C. F. Quate, *Proc. Natl. Acad. Sci. U.S.A.*, 2003, **100**, 12539-12542.
32. E. Sutter, D. P. Acharya, J. T. Sadowski and P. Sutter, *Appl. Phys. Lett.*, 2009, **94**, 133101.
33. S. Marchini, S. Gunther and J. Wintterlin, *Phys. Rev. B*, 2007, **76**, 075429.
34. E. Soy, Z. Liang and M. Trenary, *J. Phys. Chem. C*, 2015, **119**, 24796-24803.
35. L. Gao, J. R. Guest and N. P. Guisinger, *Nano Lett.*, 2010, **10**, 3512-3516.
36. P. Süle, M. Szendró, C. Hwang and L. Tapasztó, *Carbon*, 2014, **77**, 1082-1089.
37. P. Yi, Z. Haigang, S. Dongxia, S. Jiatao, D. Shixuan, L. Feng and G. Hong-jun, *Adv. Mater.*, 2009, **21**, 2777-2780.
38. E. Sutter, P. Albrecht, B. Wang, M.-L. Bocquet, L. Wu, Y. Zhu and P. Sutter, *Surf. Sci.*, 2011, **605**, 1676-1684.
39. M. Iannuzzi, I. Kalichava, H. F. Ma, S. J. Leake, H. T. Zhou, G. Li, Y. Zhang, O. Bunk, H. J. Gao, J. Hutter, P. R. Willmott and T. Greber, *Phys. Rev. B*, 2013, **88**, 125433.
40. R. Cortes, D. P. Acharya, C. V. Ciobanu, E. Sutter and P. Sutter, *J. Phys. Chem. C*, 2013, **117**, 20675-20680.
41. T. A. Land, T. Michely, R. J. Behm, J. C. Hemminger and G. Comsa, *Surf. Sci.*, 1992, **264**, 261-270.
42. P. Sutter, J. Sadowski and E. Sutter, *Phys. Rev. B*, 2009, **80**, 245411.
43. P. Merino, M. Svec, A. L. Pinardi, G. Otero and J. A. Martin-Gago, *ACS Nano*, 2011, **5**, 5627-5634.
44. J. Wintterlin and M.-L. Bocquet, *Surf. Sci.*, 2009, **603**, 1841-1852.
45. M. Batzill, *Surf. Sci. Rep.*, 2012, **67**, 83-115.
46. E. N. Voloshina, E. Fertitta, A. Garhofer, F. Mittendorfer, M. Fonin, A. Thissen and Y. S. Dedkov, *Sci. Rep.*, 2013, **3**, 1072.
47. B. Wang, M.-L. Bocquet, S. Marchini, S. Günther and J. Wintterlin, *Phys. Chem. Chem. Phys.*, 2008, **10**, 3530-3534.
48. A. L. V. de Parga, F. Calleja, B. Borca, M. C. G. Passeggi, J. J. Hinarejos, F. Guinea and R. Miranda, *Phys. Rev. Lett.*, 2008, **101**, 099703.

49. A. P. Kryukov, V. Y. Levashov and N. V. Pavlyukevich, *J. Eng. Phys. Thermophys.*, 2014, **87**, 237-245.
50. D. Appy, H. Lei, C.-Z. Wang, M. C. Tringides, D.-J. Liu, J. W. Evans and P. A. Thiel, *Prog. Surf. Sci.*, 2014, **89**, 219-238.
51. J. R. Arthur and A. Y. Cho, *Surf. Sci.*, 1973, **36**, 641-660.
52. I. Lopez-Salido, D. C. Lim and Y. D. Kim, *Surf. Sci*, 2005, **588**, 6-18.
53. R. Anton and I. Schneidereit, *Phys. Rev. B*, 1998, **58**, 13874.
54. A. R. Howells, L. Hung, G. S. Chottiner and D. A. Scherson, *Solid State Ion.*, 2002, **150**, 53-62.
55. P. W. Sutter, J.-I. Flege and E. A. Sutter, *Nat. Mater.*, 2008, **7**, 406.
56. P. Yi, Z. Haigang, S. Dongxia, S. Jiatao, D. Shixuan, L. Feng and G. Hong-jun, *Adv. Mater.*, 2009, **21**, 2777-2780.
57. K. F. McCarty, P. J. Feibelman, E. Loginova and N. C. Bartelt, *Carbon*, 2009, **47**, 1806-1813.
58. A. Lii-Rosales, Y. Zhou, M. Wallingford, C.-Z. Wang, M. C. Tringides and P. A. Thiel, *Phys. Rev. Mater.*, 2017, **1**, 026002.
59. M. Büttner, P. Choudhury, J. Karl Johnson and J. T. Yates Jr., *Carbon*, 2011, **49**, 3937-3952.
60. O. Lehtinen, J. Kotakoski, A. V. Krasheninnikov, A. Tolvanen, K. Nordlund and J. Keinonen, *Phys. Rev. B*, 2010, **81**, 153401.
61. S. Habenicht, K. P. Lieb, W. Bolse, U. Geyer, F. Roccaforte and C. Ronning, *Nucl. Instrum. Methods Phys. Res. B*, 2000, **161-163**, 958-962.
62. F. Banhart, J. Kotakoski and A. V. Krasheninnikov, *ACS Nano*, 2011, **5**, 26-41.
63. J. R. Hahn and H. Kang, *Phys. Rev. B*, 1999, **60**, 6007-6017.
64. K. F. Kelly, D. Sarkar, G. D. Hale, S. J. Oldenburg and N. J. Halas, *Science*, 1996, **273**, 1371-1373.
65. J. G. Kushmerick, K. F. Kelly, H. P. Rust, N. J. Halas and P. S. Weiss, *J. Phys. Chem. B*, 1999, **103**, 1619.
66. M. M. Ugeda, I. Brihuega, F. Guinea and J. M. Gomez-Rodriguez, *Phys. Rev. Lett.*, 2010, **104**, 096804.
67. M. M. Ugeda, I. Brihuega, F. Hiebel, P. Mallet, J.-Y. Veuillen, J. M. Gómez-Rodríguez and F. Ynduráin, *Phys. Rev. B*, 2012, **85**, 121402.
68. H. A. Mizes and J. S. Foster, *Science*, 1989, **244**, 559-562.
69. G. M. Rutter, J. N. Crain, N. P. Guisinger, T. Li, P. N. First and J. A. Stroscio, *Science*, 2007, **317**, 219-222.
70. H. González-Herrero, J. M. Gómez-Rodriguez, P. Mallet, M. Moaied, J. J. Palacios, C. Salgado, M. M. Ugeda, J.-Y. Veuillen, F. Yndurain and I. Brihuega, *Science*, 2016, **362**, 437-441.
71. J. C. M. López, M. C. G. Passeggi and J. Ferrón, *Surf. Sci.*, 2008, **602**, 671-676.
72. L. W. Yu, C. Y. Du and X. J. Liu, *Mater. Res. Express*, 2018, **5**, 025022.
73. G. D. Lee, C. Z. Wang, E. Yoon, N. M. Hwang, D. Y. Kim and K. M. Ho, *Phys. Rev. Lett.*, 2005, **95**, 205501.
74. J. Kotakoski, A. V. Krasheninnikov and K. Nordlund, *Phys. Rev. B*, 2006, **74**, 245420.
75. J. C. Meyer, C. Kisielowski, R. Erni, M. D. Rossell, M. F. Crommie and A. Zettl, *Nano Lett.*, 2008, **8**, 3582.

76. J. Kotakoski, A. V. Krasheninnikov, U. Kaiser and J. C. Meyer, *Phys. Rev. Lett.*, 2011, **106**, 105505.
77. Y. Han, A. Lii-Rosales, M. C. Tringides, J. W. Evans and P. A. Thiel, *Phys. Rev. B*, 2019, **99**, 115415.
78. C. Ronchi, M. Datteo, D. Perilli, L. Ferrighi, G. Fazio, D. Selli and C. Di Valentin, *J. Phys. Chem. C*, 2017, **121**, 8653-8661.
79. A. V. Krasheninnikov, P. O. Lehtinen, A. S. Foster, P. Pyykkö and R. M. Nieminen, *Phys. Rev. Lett.*, 2009, **102**, 126807.
80. X. Guo, S. Liu and S. Huang, *Int. J. Hydrog. Energy*, 2018, **43**, 4880-4892.
81. S. D. N., Š. Željko, B. E. N. and B. M. R., *ChemistrySelect*, 2018, **3**, 2631-2637.
82. D.-e. Jiang, B. G. Sumpter and S. Dai, *J. Chem. Phys.*, 2007, **126**, 134701.
83. Y. Han, M. C. Tringides, J. W. Evans and P. A. Thiel, *Phys. Rev. Res.*, 2020, **2**, 013182.
84. Y. Han, K. C. Lai, A. Lii-Rosales, M. C. Tringides, J. W. Evans and P. A. Thiel, *Surf. Sci.*, 2019, **685**, 48-58.
85. X.-C. Liu, S. Zhao, X. Sun, L. Deng, X. Zou, Y. Hu, Y.-X. Wang, C.-W. Chu, J. Li, J. Wu, F.-S. Ke and P. M. Ajayan, *Science Advances*, 2020, **6**, eaay4092.
86. J. A. Venables, *Phil. Mag.*, 1973, **27**, 697-738.
87. J. A. Venables, G. D. T. Spiller and M. Hanbucken, *Rep. Prog. Phys.*, 1984, **47**, 399-459.
88. J. W. Evans, P. A. Thiel and M. C. Bartelt, *Surf. Sci. Rep.*, 2006, **61**, 1-128.
89. Y. Han, A. Lii-Rosales, Y. Zhou, C. J. Wang, M. Kim, M. C. Tringides, C. Z. Wang, P. A. Thiel and J. W. Evans, *Phys. Rev. Mater.*, 2017, **1**, 053403.
90. Y. Han, A. Lii-Rosales, M. C. Tringides and J. W. Evans, *J. Chem. Phys.*, Submitted 2020.
91. M. Bartelt and J. W. Evans, *Phys. Rev. B*, 1992, **46**, 12675.
92. Y. Han, E. Gaudry, T. J. Oliveira and J. W. Evans, *J. Chem. Phys.*, 2016, **145**, 21004.
93. S. E. Julien and K.-T. Wan, *J. Appl. Mech.*, 2018, **85**, 114501.
94. K. C. Lai, A. Lii-Rosales and J. W. Evans, *J. Phys. Condens. Matter*, 2020, **32**, 445001.